

ENERGY DEPENDENCE OF SYNCHROTRON X-RAY RIMS IN TYCHO'S SUPERNOVA REMNANT

AARON TRAN (陳宏裕)^{1,4}, BRIAN J. WILLIAMS^{1,5}, ROBERT PETRE¹, SEAN M. RESSLER², STEPHEN P. REYNOLDS³

¹X-ray Astrophysics Laboratory, NASA/GSFC, Code 662, Greenbelt, MD 20771, USA

²Dept. Physics, University of California, Berkeley, CA 94720, USA

³Dept. Physics, North Carolina State University, Raleigh, NC 27695, USA

Accepted, ApJ, September 2, 2015

ABSTRACT

Several young supernova remnants exhibit thin X-ray bright rims of synchrotron radiation at their forward shocks. Thin rims require strong magnetic field amplification beyond simple shock compression if rim widths are only limited by electron energy losses. But, magnetic field damping behind the shock could produce similarly thin rims with less extreme field amplification. Variation of rim width with energy may thus discriminate between competing influences on rim widths. We measured rim widths around Tycho's supernova remnant in 5 energy bands using an archival 750 ks *Chandra* observation. Rims narrow with increasing energy and are well described by either loss-limited or damped scenarios, so X-ray rim width-energy dependence does not uniquely specify a model. But, radio counterparts to thin rims are not loss-limited and better reflect magnetic field structure. Joint radio and X-ray modeling favors magnetic damping in Tycho's SNR with damping lengths $\sim 1\text{--}5\%$ of remnant radius and magnetic field strengths $\sim 50\text{--}400\ \mu\text{G}$ assuming Bohm diffusion. X-ray rim widths are $\sim 1\%$ of remnant radius, somewhat smaller than inferred damping lengths. Electron energy losses are important in all models of X-ray rims, suggesting that the distinction between loss-limited and damped models is blurred in soft X-rays. All loss-limited and damping models require magnetic fields $\gtrsim 20\ \mu\text{G}$, affirming the necessity of magnetic field amplification beyond simple compression.

Subject headings: acceleration of particles — ISM: individual objects (Tycho's SNR) — ISM: magnetic fields — ISM: supernova remnants — shock waves — X-rays: ISM

1. INTRODUCTION

Electrons accelerated in the forward shocks of young supernova remnants (SNRs) emit synchrotron radiation strongly in the shock's immediate wake at radio wavelengths and sometimes in X-rays. In a few cases, they quickly turn off downstream, producing a shell-like morphology of bright X-ray and radio rims/filaments due to line-of-sight projection (Bamba et al. 2003; Reynoso et al. 1997). Strong and time-variable synchrotron radiation (e.g., Uchiyama et al. 2007; Patnaude & Fesen 2007), in conjunction with multiwavelength spectral modeling (Aharonian et al. 2004; Acero et al. 2010; Ackermann et al. 2013), suggests that electrons are accelerated to TeV energies in young SNRs. Although synchrotron emission due to accelerated electrons does not require acceleration of an unseen hadronic component, the prevailing theory of diffusive shock acceleration (DSA) should operate on both positive ions and electrons. Efficient hadron acceleration in supernova remnant shocks is a prime candidate source for galactic cosmic rays up to the cosmic ray spectrum's "knee" at around 3 PeV (Vink 2012). But many fundamental questions about shock acceleration remain unanswered. Under what conditions do shocks accelerate particles efficiently? How are magnetic fields amplified in such shocks? Reynolds (2008) reviews relevant observations and open questions to date. These questions are relevant to many astrophysical settings, such as Earth's bow shock (Ellison et al. 1990), starburst galaxies (Heckman et al. 1990), jets of active galactic nuclei (Chen et al. 2014), galaxy clusters (van

Weeren et al. 2010), and cosmological shocks (Ryu et al. 2008).

Spectral and spatial measurements of synchrotron rims can constrain downstream magnetic field strength and structure. If rim widths are set by electron energy losses, post-shock magnetic fields must be amplified to $\sim 10^2\ \mu\text{G}$ to account for the thinness of observed rims (Vink & Laming 2003; Bamba et al. 2003, 2005; Völk et al. 2005; Parizot et al. 2006). In these models, the magnetic field is assumed advected downstream and nearly constant over rim widths. Alternately, the magnetic field strength may be damped downstream of the shock and prevent electrons from radiating efficiently, so that thin rims reflect magnetic field variation rather than efficient particle acceleration and synchrotron cooling (Pohl et al. 2005). Damping, in particular, may permit less extreme magnetic field amplification. We refer to these as "loss-limited" and "damped" models for rim widths. We shall see that models can range continuously between these two cases, and that the distinction between the two can vary with observing frequency.

The possibility of damping in SNR shocks has not been fully tested. Marcowith & Casse (2010) compared physically motivated magnetic damping models to X-ray rim widths and synchrotron spectrum cut-offs and thus suggested that only young SNRs (age $\lesssim 500\ \text{yr}$) can exhibit magnetic damping in conjunction with efficient particle acceleration. Rettig & Pohl (2012) gave model predictions for several historical SNRs and proposed discrimination based on filament spectra – the expectation is that damped spectra are softer, loss-limited harder.

Hydrodynamic models can reproduce X-ray rim profiles reasonably well with both loss-limited and damped

⁴ CRESST/University of Maryland, College Park, MD 20742

⁵ CRESST/Universities Space Research Association

magnetic field models (Cassam-Chenaï et al. 2007; Morlino & Caprioli 2012; Slane et al. 2014). However, loss-limited models generally cannot reproduce thin radio rims. Radio-emitting GeV electrons do not lose substantial energy via radiation, so modeled intensities rise to a broad maximum toward the remnant interior, then gradually drop due to sphericity effects as the density drops in the interior. Reynolds (1988) empirically modeled radio rims in the remnant of SN 1006 and concluded that such thin rims required sharp gradients in electron energy density (from, e.g., time-variable particle acceleration) or magnetic field strength. Cassam-Chenaï et al. (2007) used a 1-D hydrodynamic model with nonlinear DSA to jointly model radio and X-ray rims in Tycho’s supernova remnant; neither loss-limited nor damped models could match radio profiles and radio/X-ray intensities simultaneously. Moreover, gradual X-ray spectral variation observed downstream of the shock front was poorly reproduced with both models (Cassam-Chenaï et al. 2007). But damped models were able generate limb-brightened radio rims at the forward shock, even if morphology was not entirely consistent with observation. Cassam-Chenaï et al. (2007) thus suggested that some combination of amplification and magnetic field variation might explain radio morphology.

Recently, Ressler et al. (2014) (hereafter, R14) sought to discriminate between damped and loss-limited rims by measuring rim width-energy dependence in X-ray energies in SN 1006. In the simplest models, rim widths are expected to be roughly energy-independent if rims are damped, whereas widths should narrow with increasing energy if rims are energy loss-limited. R14 included a variety of effects which can blur this distinction. To further test these models, we follow R14 by measuring X-ray rim widths at multiple energies in Tycho’s supernova remnant (hereafter, Tycho). Tycho exhibits an extensive shell of synchrotron-dominated thin rims around its periphery (Figure 1); the rims show very little thermal emission, consistent with expansion into a low density ISM (Williams et al. 2013). A deep 750 ks exposure of the entire remnant from 2009 allows fine sampling of the remnant rims. We build upon previous estimates of magnetic field strength and particle diffusion in Tycho that draw from multiwavelength observations and various assumptions on CR acceleration (Völk et al. 2002, 2005; Parizot et al. 2006; Morlino & Caprioli 2012; Rettig & Pohl 2012, e.g.,).

Our procedure closely follows that of R14. We first review the model of R14 used to model rim profiles and widths, then describe the procedure for selecting, measuring, and fitting rim widths to model width-energy dependence. We explore degeneracies in model fitting and consider radio rim morphology as an additional discriminant between models.

2. NONTHERMAL RIM MODELING

2.1. Particle transport

The energy and space distribution of electrons at a supernova remnant’s forward shock controls the synchrotron rims we see in X-ray and radio. We assume that diffusive shock acceleration generates a power law distribution of electrons with an exponential cut-off at the forward shock and model 1-D steady-state plane ad-

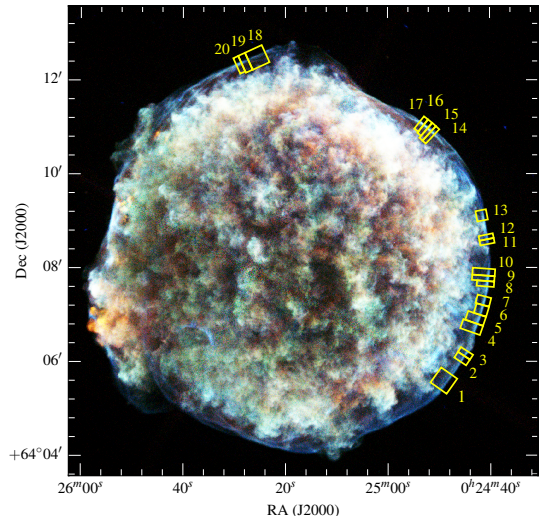


Figure 1. RGB image of Tycho with region selections overlaid. Image bands are 0.7–1 keV (red), 1–2 keV (green) and 2–7 keV (blue). Bold region labels (1, 16) indicate region selections shown in Figures 3, 4. Filament 1: Regions 1–3, filament 2: regions 4–10, filament 3: regions 11–13, filament 4: regions 14–17, filament 5, regions 18–20.

vection and diffusion of the electron distribution $f(E, x)$, where E is electron energy and x is distance downstream of the forward shock:

$$v_d \frac{\partial f}{\partial x} - \frac{\partial}{\partial x} \left(D \frac{\partial f}{\partial x} \right) - \frac{\partial}{\partial E} (b B^2 E^2 f) = K_0 E^{-s} e^{-E/E_{\text{cut}}} \delta(x), \quad (1)$$

following Berezhko & Völk (2004); Cassam-Chenaï et al. (2007); Morlino et al. (2010); Rettig & Pohl (2012). The forward shock is located at $x = 0$ with $x > 0$ increasing downstream of the shock; D is the diffusion coefficient, v_d is fluid velocity downstream of the shock, and the constant $b \equiv 4e^4/9m_e^4c^7 = 1.57 \times 10^{-3}$ in appropriate CGS units arises from synchrotron power loss (i.e., $\partial E/\partial t = -b B^2 E^2$, averaged over pitch angles). The initial electron distribution is specified by an arbitrary normalization K_0 , DSA cut-off energy E_{cut} (given in Section 2.3), and spectral index $s = 2\alpha + 1$. Zirakashvili & Aharonian (2007) derive an electron energy spectrum with super-exponential cut-off $e^{-(p/p_{\text{cut}})^2}$, but we use a simple exponential cut-off for simplicity and consistency with R14. We have not yet specified the cause of the injected spectrum cut-off (see Section 2.4), but the functional form of a power law with exponential cut-off is a good approximation to predictions for DSA spectra limited by synchrotron losses, remnant age, or particle escape (Webb et al. 1984; Reynolds 1998, 2008). All constants and equations are given in CGS (Gaussian) units. Our presentation is somewhat abbreviated, but a fuller exposition and literature review are given by R14.

For Tycho, we adopted radio spectral index $\alpha = 0.58$ (Sun et al. 2011) and hence electron spectral index $s = 2\alpha + 1 = 2.16$. We assumed a remnant distance 3 kpc (but cf. Hayato et al. 2010), which gives a shock radius of 1.08×10^{19} cm from the observed angular radius $240''$ (Green 2014) and further sets shock velocities for each rim profile we consider. Tycho’s forward shock velocity varies with azimuth by up to a factor of 2 (Katsuda

et al. 2008); we linearly interpolated velocities reported by Williams et al. (2013) (rescaled to 3 kpc) to estimate individual shock velocities for each region. We assume a compression ratio of 4 as for a strong shock (unmodified by cosmic-ray pressure), and take downstream velocities v_d to be one-fourth the interpolated shock velocities.

We assume isotropic diffusion and only consider particle transport downstream of the forward shock. The velocity is assumed constant, as is the magnetic field for loss-limited model rims, in contrast to the expected Sedov-Taylor similarity solution for velocity and density in an adiabatic blastwave. Our assumptions of constant velocity, magnetic field, and plane flow should be reasonable as we generally consider synchrotron emission within 10% of the shock radius, r_s , from the forward shock, though a few models are followed far enough inward that this approximation begins to break down. We consider profile emission strictly upstream of both the contact discontinuity and reverse shock (cf. Warren et al. 2005), and avoid regions where the contact discontinuity overruns the forward shock. Our modeling neglects flow and electron spectrum modification due to the nearby contact discontinuity and particle acceleration at the reverse shock. These effects could matter (and we do not quantify their importance), but we expect that at Tycho's age, X-ray emission is dominated by forward shock transport. Given the uncertainty in shock morphology, our model seeks only to capture the most relevant physics. More sophisticated work may treat, e.g., sphericity, shock precursors, anisotropic diffusion, and injection/acceleration efficiency (e.g., Reville & Bell 2013; Bykov et al. 2014; Ferrand et al. 2014, and references therein).

To determine rim profiles and widths, we compute the electron distribution using Green's function solutions by Lerche & Schlickeiser (1980) and Rettig & Pohl (2012), with the caveat that $D(x)B^2(x)$ is assumed constant; we discuss this assumption further below. The solutions are fully described in R14 using notation similar to ours. The electron distribution may be integrated over the one-particle synchrotron emissivity $G(y)$ to obtain the "total" emissivity:

$$j_\nu(x) \propto \int_0^\infty G(y)f(E, x)dE \quad (2)$$

where $y \equiv \nu/(c_1 E^2 B)$ is a scaled synchrotron frequency and $G(y) = y \int_y^\infty K_{5/3}(z)dz$ with $K_{5/3}(z)$ a modified Bessel function of the second kind (Pacholczyk 1970); the constant $c_1 = 6.27 \times 10^{18}$ in CGS units. Integrating emissivity over lines of sight for a spherical remnant yields intensity as a function of radial coordinate r :

$$I_\nu(r) = 2 \int_0^{\sqrt{r_s^2 - r^2}} j_\nu(r_s - \sqrt{s^2 + r^2}) ds \quad (3)$$

where s is the line-of-sight coordinate and r_s is shock radius. We take the full width at half maximum (FWHM) of the resulting intensity profile as our metric for modeled rim widths. Using FWHM as opposed to, e.g., full width at three-quarters maximum, excludes measured rims and model parameters where X-ray intensity does not drop to half maximum immediately behind the rim. Our results thus focus on the most well-defined rims in Tycho rather than the global shock structure.

2.2. Magnetic fields and damping

We consider two scenarios for post-shock magnetic field: (1) a constant field $B(x) = B_0$ corresponding to loss-limited rims, and (2) an exponentially damped field of form:

$$B(x) = (B_0 - B_{\min}) \exp(-x/a_b) + B_{\min} \quad (4)$$

following (Pohl et al. 2005). Here B_0 is the magnetic field immediately downstream of the shock, i.e. $B_0 = B(x=0)$, and a_b is an e -folding damping lengthscale; our use of B_0 for downstream magnetic field departs from typical notation. A typical lengthscale for a_b is 10^{16} to 10^{17} cm (Pohl et al. 2005), corresponding to ~ 0.1 – 1% of Tycho's radius. Hereafter, we report a_b in units of shock radius r_s unless otherwise stated.

The distinction between damped and loss-limited rims is somewhat arbitrary; as $a_b \rightarrow \infty$, model results converge to loss-limited rims. Moreover, rims much thinner than the damping length are effectively loss-limited as electrons radiate in a nearly constant magnetic field. Furthermore, the dependence on observing frequency of electron losses and diffusion means that a model may be damping limited at one frequency and loss-limited at another. In the following analysis, we deem all fits with finite a_b to be damped, but we compare rim widths and damping lengths from such fits further below to better distinguish damped and loss-limited rim behavior, set by a combination of a_b , B_0 , and other model parameters.

2.3. Diffusion coefficient

Most previous work has assumed Bohm-like diffusion in plasma downstream of SNR shocks. Bohm diffusion assumes that the particle mean free path λ is equal to the gyroradius $r_g = E/(eB)$, yielding diffusion coefficient $D_B = \lambda c/3 = cE/(3eB)$; here c is the speed of light, E is particle energy, e is the elementary charge, and B is magnetic field. Bohm-like diffusion encapsulates diffusion scalings of $D \propto E$, introducing a free prefactor η such that $\lambda = \eta r_g$ allows for varying diffusion strength. However, Bohm diffusion at $\eta = 1$ is commonly considered a lower limit on the diffusion coefficient at all energies.

We consider a generalized diffusion coefficient with arbitrary power law dependence upon energy following, e.g., Parizot et al. (2006):

$$D(E) = \frac{\eta c E^\mu}{3eB} = \eta_h D_B(E_h) \left(\frac{E}{E_h} \right)^\mu \quad (5)$$

where μ parameterizes diffusion-energy scaling and η now has units of $\text{erg}^{1-\mu}$. The right-hand side of equation (5) introduces η_h , a dimensionless diffusion coefficient scaled to the Bohm value at a fiducial particle energy E_h . Note that η_h and η are related as $\eta = \eta_h (E_h)^{1-\mu}$, and $\eta = \eta_h$ for Bohm-like diffusion ($\mu = 1$). For subsequent analysis, we take fiducial electron energy $E_2 = E_h$ corresponding to a 2 keV synchrotron photon and report results in terms of $\eta_2 = \eta_h$. Although E_2 varies with magnetic field as $E_2 \propto B^{-1/2}$ and thus η_2 may vary around Tycho's shock for $\mu \neq 1$, tying η_h to a fixed observation energy gives a convenient sense of diffusion strength regardless of the underlying electron energies.

The solutions to equation (1) given by Lerche & Schlickeiser (1980) assume $D(x)B^2(x)$ constant to ren-

der equation (1) semi-analytically tractable. Although this assumption has no obvious physical basis, it contains the qualitatively correct behavior D constant if B is constant and D smaller for larger B . We enforce it by modifying the diffusion coefficient in the damping model as, following Rettig & Pohl (2012):

$$D(E, x) = \frac{\eta c E^\mu}{3eB_0} \left[\frac{B_{\min}}{B_0} + \frac{B_0 - B_{\min}}{B_0} e^{-x/a_b} \right]^{-2}. \quad (6)$$

This strengthens the spatial-dependence of the diffusion coefficient as compared to the expected $D(x) \propto 1/B(x)$.

2.4. Electron energy cut-off

We assume that the DSA process is limited by synchrotron losses at high energies and hence determine the E_{cut} by equating synchrotron loss and diffusive acceleration timescales. Here we ignore the possibility of age-limited or escape-limited acceleration (e.g., Reynolds 1998). In the former case, low magnetic-field strengths could mean that Tycho's age is less than a synchrotron loss time; the maximum energy is obtained by equating the remnant age and acceleration timescale. In the latter case, the diffusion coefficient upstream may increase substantially above some electron energy due to an absence of appropriate MHD waves. However, the magnetic field strengths we find below justify the assumption of loss-limited acceleration. For low energies and small synchrotron losses (cooling time longer than acceleration time), electrons are efficiently accelerated; near or above the cut-off energy, electrons will radiate or escape too rapidly to be accelerated to higher energies and the energy spectrum drops off steeply. The cut-off energy is given as:

$$E_{\text{cut}} = (8.3 \text{ TeV})^{2/(1+\mu)} \left(\frac{B_0}{100 \mu\text{G}} \right)^{-1/(1+\mu)} \times \left(\frac{v_s}{10^8 \text{ cm s}^{-1}} \right)^{2/(1+\mu)} \eta^{-1/(1+\mu)}. \quad (7)$$

This result is derived by Parizot et al. (2006) for $\mu = 1$ assuming a strong shock with compression ratio 4 and isotropic magnetic turbulence both upstream and downstream of the shock.

The cut-off energy and accelerated electron spectrum depend on the magnetic field, which varies in a damped model. Marcowith & Casse (2010) show that various turbulent damping mechanisms can modify the accelerated spectrum, as particles traveling downstream may not be effectively reflected back across the shock and further accelerated. Nevertheless, we make the simplifying assumption that particle acceleration is controlled by diffusion at the shock and neglect spatially varying diffusion and magnetic fields in the acceleration process; equation (7) stands as evaluated with shock magnetic field strength B_0 . Cut-off energies of ~ 1 – 10 TeV can be plausibly achieved in the presence of damping due to Alfvén and magneto-sonic cascades (Marcowith & Casse 2010).

As the DSA imposed electron cut-off results in a cut-off of SNR synchrotron flux, the synchrotron cut-off frequency $\nu_{\text{cut}} = c_m E_{\text{cut}}^2 B$ with $c_m = 1.82 \times 10^{18}$ in cgs units (e.g. Pacholczyk 1970), which is the peak frequency emitted by electrons of energy E_{cut} , provides an independent

observable to estimate shock diffusion and is given by:

$$\nu_{\text{cut}} = c_m (13.3 \text{ erg})^{\frac{4}{1+\mu}} (100 \mu\text{G}) (2657 \text{ erg}^2)^{-\frac{1-\mu}{1+\mu}} \times \left(\frac{v_s}{10^8 \text{ cm/s}} \right)^{\frac{4}{1+\mu}} (\eta_2)^{-\frac{2}{1+\mu}}. \quad (8)$$

The cut-off frequency is independent of magnetic field B for all values of μ (but recall that the electron energies associated with η_2 will depend on B for $\mu \neq 1$). Parizot et al. (2006) previously used measurements of synchrotron cut-offs to estimate diffusion coefficients in Tycho and other historical supernova remnants.

We point out that the electron spectrum softens downstream of the shock due to synchrotron losses, but the local spectrum at any radial position will be a steeply cut-off power law (Webb et al. 1984; Reynolds 1998). No steepening from E^{-s} to $E^{-(s+1)}$ is observed because the cut-off limits the electron spectrum at high energies. A homogeneous source of age t in which electrons are continuously accelerated throughout, with an initial straight power law distribution to infinite energy, will produce a steepened power law distribution above the energy at which the synchrotron loss time equals the acceleration time (Kardashev 1962). If we model emission without an initial exponential cut-off (i.e., inject a straight power law) in a constant magnetic field, then integrated spectra in our model would steepen by about one power. But, those assumptions do not apply to the current situation of continuous advection of electrons, with an energy distribution which is already a cut-off power law, through a region of non-constant magnetic field. See Reynolds (2009) for a fuller discussion of synchrotron losses in non-homogeneous sources.

2.5. Rim width-energy dependence

X-ray rim widths are controlled by synchrotron losses, particle transport, and magnetic fields immediately downstream of the shock, each of which influences rim width-energy scaling differently. If diffusion is negligible and the downstream magnetic field is constant, loss-limited rims narrow with increasing energy as more energetic electrons radiate and cool more quickly. But diffusion will dilute this effect: more energetic electrons may diffuse further upstream or downstream than would be expected from pure advection, smearing out rims and weakening energy dependence at higher energies. Magnetic fields damped on a length scale comparable to filament widths should also weaken rim width-energy dependence – if the magnetic field turns off, synchrotron radiation turns off regardless of electron energy. Additionally, once B_0 varies, one observes electrons of different energy at different distances behind the shock.

Figure 2 plots model X-ray and radio profiles for a range of B_0 and a_b values to illustrate how damping and magnetic field strength impact width-energy dependence, which we will now explore. We discuss and incorporate model radio profiles into our analysis in Section 6.

2.5.1. Undamped models

Following R14, we parameterize rim width-energy dependence in terms of a scaling exponent m_E defined as:

$$w(\nu) \propto \nu^{m_E} \quad (9)$$

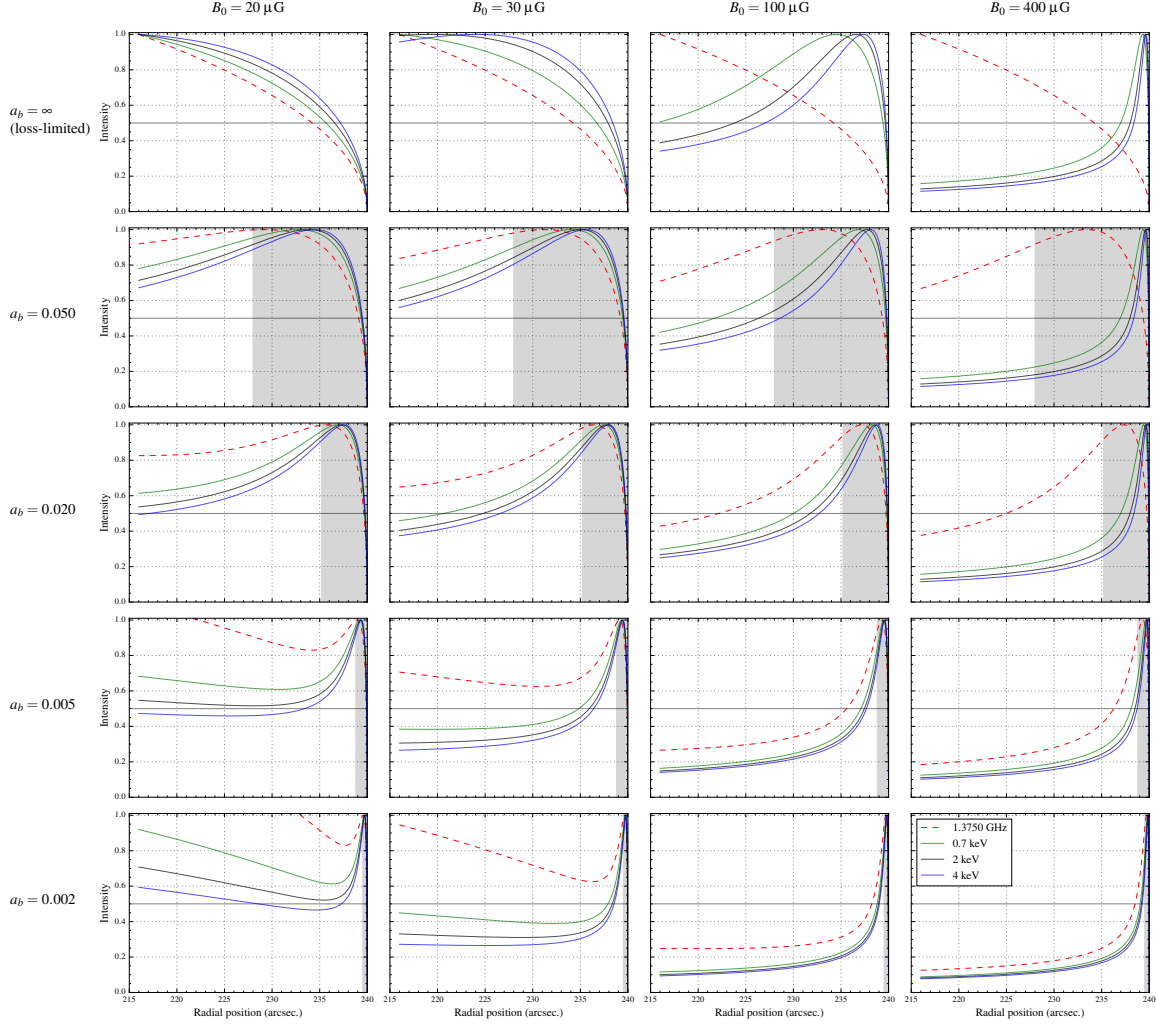


Figure 2. Radio and X-ray rim profiles for a range of magnetic fields (B_0) and damping lengths (a_b , shaded regions) with $\mu = 1$, $\eta_2 = 1$, and $B_{\min} = 5 \mu\text{G}$ fixed. X-ray rim energies (0.7, 2, 4 keV) are representative of energy bands used in our rim width measurements. This plot summarizes several key features of our model: (1) radio profiles (dashed red) are strongly affected by damping for all values of B_0 because synchrotron losses are negligible at low electron energies. (2) X-ray profiles (solid green, black, blue) are influenced by synchrotron losses even in the presence of strong damping, which can be seen going from left to right (increasing B_0). (3) When X-ray rim widths are smaller than a_b , field damping only weakly affects rim widths and width-energy dependence (top right panels). (4) Strongly damped X-ray rims can show significant width-energy dependence in our model due to synchrotron losses beyond a_b . This occurs for smaller B_0 where the contrast between B_0 and B_{\min} is less extreme (bottom left panels).

where $w(\nu)$ is filament FWHM as a function of observed photon frequency ν , and the exponent $m_E = m_E(\nu)$ is energy dependent. We may refer to observed photons interchangeably by energy or frequency ν , but E is reserved for electron energy.

To better intuit the effects of advection and diffusion on rim widths, we introduce advective and diffusive lengthscales for bulk electron transport. These depend on electron energy; we write them in terms of the peak frequency radiated by electrons of energy E , $\nu = c_m E^2 B$.

$$l_{\text{ad}} = v_d \tau_{\text{synch}} \propto v_d B_0^{-3/2} \nu^{-1/2} \quad (10)$$

$$l_{\text{diff}} = \sqrt{D \tau_{\text{synch}}} \propto \eta^{1/2} B_0^{-(\mu+5)/4} \nu^{(\mu-1)/4} \quad (11)$$

The characteristic time is the synchrotron cooling time $\tau_{\text{synch}} = 1/(bB^2E)$ with $b = 1.57 \times 10^{-3}$. For $\mu = 1$, l_{diff} is independent of ν and both l_{diff} and l_{ad} scale as $B_0^{-3/2}$. If both diffusion and magnetic field damping are negligible and electrons are only loss-limited as they advect

downstream, m_E attains a minimum value $m_E = -1/2$ as rim widths are set by $l_{\text{ad}} > l_{\text{diff}}$. At higher energies where $l_{\text{diff}} > l_{\text{ad}}$, diffusion increases m_E from $-1/2$ to a value between $-1/4$ and $1/4$ for $\mu = 0$ and 2 respectively (R14, Figure 3). The presence of an electron energy cut-off decreases m_E slightly in all cases due to the decreased number of electrons and hence thinner rims at higher energies (R14, Figure 5), but the qualitative behavior is the same.

2.5.2. Field damping effects

We expect magnetic damping to produce comparatively energy-independent rim widths. If synchrotron rim widths are set by magnetic damping at some observation energy, then rims will be damped at all lower observation energies as well. Then rim widths will be relatively constant (small $|m_E|$) below a threshold energy and may decrease, or even increase once advection and/or diffusion control rim widths at higher photon en-

ergies (advection: $l_{\text{ad}} < a_b$; diffusion: $l_{\text{diff}} > l_{\text{ad}}, a_b$). Thus, we intuit that rim widths should roughly scale as $w \sim \min(a_b, \max(l_{\text{ad}}, l_{\text{diff}}))$. This is correct except for one key region of parameter space: strong damping with weak magnetic field amplification, where synchrotron losses downstream of the FWHM create energy dependent widths even when $a_b \ll l_{\text{ad}}, l_{\text{diff}}$.

This counter-intuitive energy dependence for strongly damped models occurs when rim brightness remains above half-maximum within $\sim a_b$ of the shock. Farther downstream, synchrotron losses in the reduced magnetic field $\sim B_{\text{min}}$ drive intensity down to half-maximum; losses in a nearly constant field cause energy dependence despite magnetic damping at the shock. Synchrotron losses far from the shock will only affect the spectrum at higher frequencies; at lower frequencies, the spectrum will be effectively constant after the magnetic field’s initial decay. Thus, there will be a characteristic frequency below which the FWHM ceases to be defined. The energy dependence of rim FWHMs becomes large and diverges near this frequency. The characteristic frequency and value of m_E are sensitive to our definition of rim width (FWHM), but the physical behavior we describe (divergence of m_E at characteristic frequency, for appropriate damping parameters) will occur regardless of our definition of rim width.

3. OBSERVATIONS

3.1. Data and region selections

We measured synchrotron rim full widths at half maximum (FWHMs) from an archival *Chandra* ACIS-I observation of Tycho (RA: 00^h25^m19^s.0, dec: +64°08′10″.0; J2000) between 2009 Apr 11 and 2009 May 5 (PI: J. Hughes; ObsIDs: 10093–10097, 10902–10906); Eriksen et al. (2011) present additional observation information. The total exposure time was 734 ks. Level 1 *Chandra* data were reprocessed with CIAO 4.6 and CALDB 4.6.1.1 and kept unbinned with ACIS spatial resolution 0.492″. Merged and corrected events were divided into five energy bands: 0.7–1 keV, 1–1.7 keV, 2–3 keV, 3–4.5 keV, and 4.5–7 keV. We excluded the 1.7–2 keV energy range to avoid Si XIII (He α) emission prevalent in the remnant’s thermal ejecta which might contaminate our nonthermal profile measurements.

We selected 20 regions for profile extraction around Tycho’s shock (Figure 1) based on the following criteria: (1) filaments should be clear of spatial plumes of thermal ejecta in *Chandra* images, which rules out, e.g., areas of strong thermal emission on Tycho’s eastern limb; (2) filaments should be singular and localized, so multiple filaments should either not overlap or completely overlap; (3) filament peaks should be evident above the background signal or downstream thermal emission (rules out faint southern filaments). We accepted several regions with poor quality peaks in the lowest energy band (0.7–1 keV) so long as peaks in all higher energy bands were clear and well-fit. We grouped regions into 5 filaments by visual inspection of the remnant. Within each filament, we chose region widths to obtain comparable counts at the thin rim peak. All measured rim widths are at least 1″. The narrowest rim widths may be slightly over-estimated due to the *Chandra* point-spread function (PSF) at $\sim 4'$ off the optical axis, which has FWHM

$\leq 1.4''$ at 6.4 keV and $\leq 1''$ at 1.5 keV. For simplicity, we neglect PSF effects in our analysis. Our observations of rim width-energy dependence are thus somewhat conservative at the highest energy

3.2. Filament spectra

We extracted spectra at and immediately behind thin rims in each region (“rim”, “downstream” spectra respectively) to confirm that rim width measurements are not contaminated by thermal line emission. The two extraction regions are determined by our empirical fits of rim profile shape (Section 3.3). The rim section is the smallest sub-region containing the measured FWHM bounds from all energy bands. The downstream section extends from the interior thin rim FWHM to the intensity minimum behind the rim (specifically, the downstream profile fit domain bound described in Section 3.3). To illustrate our selections, Figure 3 plots example rim profiles (4.5–7 keV) with the downstream and rim sections highlighted.

Spectra were binned to a minimum of 15 cts/bin. We extracted background spectra from circular regions (radius $\sim 30''$) around the remnant’s exterior; for each region’s rim and downstream spectra, we subtracted the closest background region’s spectrum.

We fit each region’s rim and downstream spectra to an absorbed power law model (XSPEC 12.8.1, `phabs*powerlaw`) between 0.5–7 keV with photon index Γ , hydrogen column density N_H , and a normalization as free parameters. Table 1 lists best fit parameters and reduced χ^2 values for all regions. Rim spectra are well-fit by the power law model alone; the best fit photon indices (2.4–3) and column densities ($0.6\text{--}0.8 \times 10^{22} \text{ cm}^{-2}$) are consistent with previous spectral fits to Tycho’s non-thermal rims (Hwang et al. 2002; Cassam-Chenaï et al. 2007).

Downstream spectra are poorly fit by the absorbed power law model due to thermal contamination from Si XIII and S XV He α line emission at 1.85 and 2.45 keV. To confirm that thermal emission is dominated by these two lines near the shock, we also performed fits with (1) both lines excised (1.7–2.0 keV, 2.3–2.6 keV counts removed) and (2) with both lines fitted to Gaussian profiles. Fits with lines excised yield χ^2_{red} values between 1–5. Fits with lines fitted to Gaussian profiles yield χ^2_{red} values 0.83–1.6. In both fits (lines excised or modeled), we find somewhat smaller best fit column densities ($0.3\text{--}0.8 \times 10^{22} \text{ cm}^{-2}$) but similar best fit photon indices (2.6–3.1), compared to those of the rim spectra. The consistent photon indices indicate that the same synchrotron continuum is present beneath thermal line emission.

We also fitted “rim” spectra (Section 3.2) to the absorbed XSPEC model `srcut`, modified to fit in log-frequency space. `srcut` models a power law X-ray synchrotron spectrum set by a radio spectral index α with an exponential cut-off parameterized by cut-off frequency ν_{cut} (Reynolds 1998; Reynolds & Keohane 1999). The fit values of ν_{cut} , in particular, permit an independent estimate of η_2 from equation (8). The radio spectral index is fixed to $\alpha = 0.58$ (Sun et al. 2011) as done in our transport modeling, and we fit for absorption column density N_H and cut-off frequency ν_{cut} in each region. Table 1 lists best spectrum fit parameters for each region. The

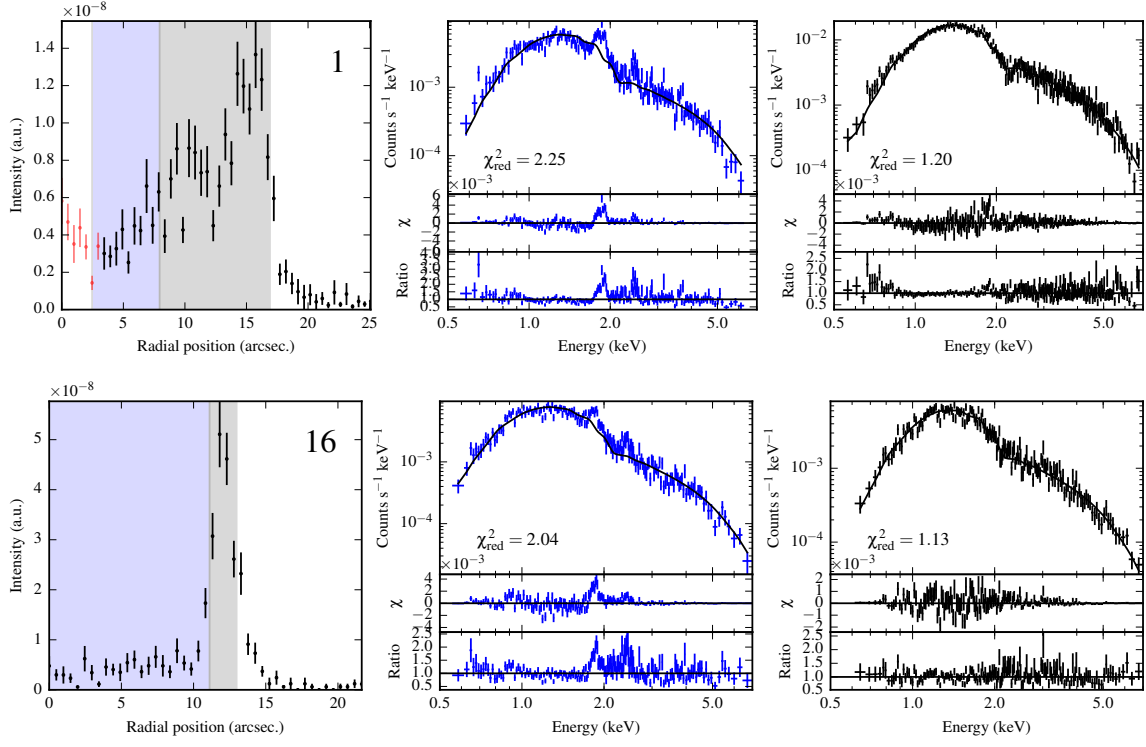


Figure 3. Spectra and fits from Regions 1 (top) and 16 (bottom) show varying rim morphology; Region 1 shows a rim where the 0.7–1 keV peak could not be fit. Left: 4.5–7 keV profiles with downstream (blue) and rim (grey) sections highlighted. Intensity is in arbitrary units (a.u.). Middle: downstream spectra with absorbed power law fit; Si and S lines at 1.85, 2.45 keV are clearly visible. Right: rim spectra with absorbed power law fit show that rims in each region are likely free of thermal line emission.

Table 1
Absorbed power law spectrum fit parameters

Region	Downstream, power-law			Rim, power-law			Rim, <code>srcut</code>		
	N_{H} (10^{22} cm^{-2})	Γ (-)	χ^2_{red} (dof)	N_{H} (10^{22} cm^{-2})	Γ (-)	χ^2_{red} (dof)	N_{H} (10^{22} cm^{-2})	ν_{cut} (keV/h)	χ^2_{red} (dof)
1	0.53	2.72	2.25 (186)	0.72	2.84	1.20 (284)	0.62	0.30	1.17 (284)
2	0.68	2.99	5.07 (178)	0.69	2.83	1.10 (202)	0.60	0.30	1.08 (202)
3	0.67	2.96	1.97 (186)	0.77	2.80	1.15 (167)	0.68	0.33	1.14 (167)
4	0.59	2.97	1.43 (163)	0.70	2.84	1.21 (278)	0.61	0.29	1.15 (278)
5	0.62	2.93	4.76 (265)	0.73	2.88	1.18 (255)	0.64	0.27	1.11 (255)
6	0.68	3.00	2.12 (200)	0.74	2.85	0.96 (231)	0.64	0.29	0.93 (231)
7	0.65	3.02	1.00 (142)	0.82	2.97	1.14 (224)	0.71	0.23	1.14 (224)
8	0.74	2.93	1.38 (170)	0.75	2.71	0.98 (198)	0.66	0.41	0.96 (198)
9	0.78	3.03	1.12 (157)	0.82	2.83	0.90 (175)	0.73	0.30	0.88 (175)
10	0.62	2.86	1.40 (220)	0.77	2.76	0.98 (164)	0.68	0.36	0.96 (164)
11	0.67	2.94	2.56 (137)	0.69	2.60	1.10 (153)	0.61	0.55	1.07 (153)
12	0.61	2.79	2.65 (137)	0.64	2.44	0.90 (172)	0.57	0.88	0.90 (172)
13	0.61	2.98	3.12 (198)	0.67	2.73	1.12 (235)	0.59	0.38	1.09 (235)
14	0.46	2.93	1.37 (148)	0.63	2.93	0.96 (167)	0.54	0.23	0.95 (167)
15	0.43	2.92	1.33 (150)	0.65	2.84	1.05 (183)	0.57	0.29	1.03 (183)
16	0.48	2.94	2.04 (189)	0.67	2.80	1.13 (182)	0.58	0.32	1.12 (182)
17	0.48	2.86	1.70 (188)	0.68	2.83	0.97 (187)	0.59	0.30	0.94 (187)
18	0.44	2.87	1.91 (200)	0.64	3.02	1.20 (220)	0.55	0.19	1.13 (220)
19	0.40	2.84	1.31 (133)	0.66	2.78	1.01 (157)	0.57	0.34	0.99 (157)
20	0.40	2.75	3.01 (140)	0.63	2.81	1.11 (192)	0.55	0.31	1.07 (192)

Note. — Absorbed power law fit parameters are photon index Γ and hydrogen column density N_{H} . `srcut` fits performed in log-frequency space; h is Planck's constant and ν_{cut} a cut-off frequency. Horizontal rules group individual regions into filaments.

fitted cut-off frequency is typically 0.3 keV/h, consistent with fits by Hwang et al. (2002), but Regions 11, 12 have unusually high cut-off frequencies 0.55, 0.88 keV/h consistent with harder rim spectra.

Our spectral fitting confirms that all selected region are practically free of thermal line emission, as already suggested by visual inspection (Figure 1). Excluding 1.7–2 keV photons in rim width measurements further limits thermal contamination as 1.85 keV Si line emission is over a third of Tycho’s thermal flux as detected by *Chandra* (Hwang et al. 2002).

3.3. Filament width measurements

We obtained radial intensity profiles in five energy bands from ~ 10 – $20''$ behind the shock to ~ 5 – $10''$ in front for each region. To increase signal-to-noise, we integrate along the shock (5 – $23''$) in each region. Plotted and fitted profiles are reported in vignetting and exposure-corrected intensity units; error bars were computed from raw counts assuming Poisson statistics. Intensity profiles peak sharply within ~ 2 – $3''$ behind the shock, demarcating the thin rims, then fall off gradually until thermal emission picks up further behind the shock.

We fitted rim profiles to a piecewise two-exponential model:

$$h(r) = \begin{cases} A_u \exp\left(\frac{r_0 - r}{w_u}\right) + C_u, & r \geq r_0 \\ A_d \exp\left(\frac{r - r_0}{w_d}\right) + C_d, & r < r_0 \end{cases} \quad (12)$$

where $h(r)$ is profile height and r is radial distance from remnant center. The rim model has 6 free parameters: A_u, r_0, w_u, w_d, C_u , and C_d ; $A_d = A_u + (C_u - C_d)$ enforces continuity at $r = r_0$. Our model is similar to that of Bamba et al. (2003, 2005) and differs slightly from that of R14. To fit only the nonthermal rim in each intensity profile, we selected the fit domain for each profile as follows. The downstream bound was set at the first local data minimum downstream of the rim peak, identified by smoothing the profiles with a 21-point ($\sim 10''$) Hanning window. The upstream bound was set at the profile’s outer edge. Figure 4 illustrates the fit domain selections for two example regions.

From the fitted profiles we extracted a full width at half maximum (FWHM) for each region and each energy band after subtracting a constant background term $\min(C_u, C_d)$. We could not resolve a FWHM in 8 of 20 regions at 0.7–1 keV (Table 2); in these regions, either the downstream FWHM bound would extend outside the fit domain or we could not find an acceptable fit to equation (12). We were able to resolve FWHMs for all regions at higher energy bands (1–7 keV).

To estimate FWHM uncertainties, we horizontally stretched each best fit profile by mapping radial coordinate r to $r'(r) = r(1 + \xi(r - r_0)/(50'' - r_0))$ with ξ an arbitrary stretch parameter and r_0 the best fit rim center from equation (12), yielding a new profile $h'(r) = h(r'(r))$. We varied ξ (and hence rim FWHM) to vary each profile fit χ^2 by 2.7 and took stretched FWHMs as upper/lower bounds on reported FWHMs. This procedure again follows R14.

3.4. Filament model fitting

We fit model FWHM predictions given by equation (1) to measured rim widths as a function of energy by varying several physical parameters: magnetic field strength B_0 , normalized diffusion coefficient η_2 , diffusion-energy scaling exponent μ , and minimum field strength B_{\min} and lengthscale a_b for a damped magnetic field. We mapped each width measurement to the lower energy limit of its energy band; e.g., 0.7–1 keV is assigned to 0.7 keV and fitted to model profile widths at 0.7 keV. Width errors in our least squares fits average the positive and negative errors on each FWHM measurement. For a given set of model parameters, we numerically computed intensity profiles and hence model FWHMs as detailed in Section 2.1; we then used a Levenberg-Marquardt fitter to seek model parameters yielding best fit FWHMs. To assist the nonlinear fitting, we tabulated model FWHM values on a large grid of model parameters and used best fit grid parameters as initial guesses for fitting. We required η_2 to be positive and deemed best fit values with $\eta_2 \geq 10^5$ and $B_0 \geq 10$ mG to be effectively unconstrained. In subsequent analysis we focus on fits with $\mu = 1$ and $\eta_2 = 1$ fixed, though we discuss the effects of varying both μ and η_2 (and fitting for η_2) as well (recall that for $\mu = 1$, η is energy-independent).

The purely loss-limited model (constant downstream magnetic field B_0) has three parameters μ , η_2 , and B_0 . To make nonlinear fitting tractable, we fixed μ in all fits and considered $\mu = 0, 1/3, 1/2, 1, 1.5$, and 2. In particular, nonlinear diffusion-energy scalings with $\mu = 1/3$ and $1/2$ may arise from Kolmogorov and Kraichnan turbulent energy spectra respectively (Reynolds 2004).

For damped magnetic field fits, we held the remnant interior field strength B_{\min} constant at 5 μ G, slightly higher than typical intergalactic values of ~ 2 –3 μ G (Lyne & Smith 1989; Han et al. 2006). We stepped a_b through 14 different values between 0.5 and 0.002 (sampling most finely between 0.01 and 0.002). To ensure that damped fits generate rims influenced by magnetic damping, we arbitrarily require that the rim FWHM at 2 keV be strictly greater than the fit value of a_b ; we revisit this requirement below. For best fits, we report the value of a_b yielding the smallest χ^2 value, with the caveat that our a_b sampling is relatively coarse.

Predicted rim widths are subject to resolution error in the numerical integrals (discretization over radial coordinate, line-of-sight coordinate, electron distribution, Green’s function integrals). We chose integration resolutions such that the fractional error in model FWHMs associated with halving or doubling each integration resolution is less than 1% for the parameter space relevant to our filaments. The maximum resolution errors in a sample of parameter space are typically 0.1–1%, but mean and median errors are typically an order of magnitude smaller than maximum errors.

4. RESULTS

4.1. Rim widths

Measured rim widths decrease with energy in most regions and energy bands. Table 2 reports FWHM measurements for all of our regions. We also report m_E values for all but the lowest energy band, computed point-to-

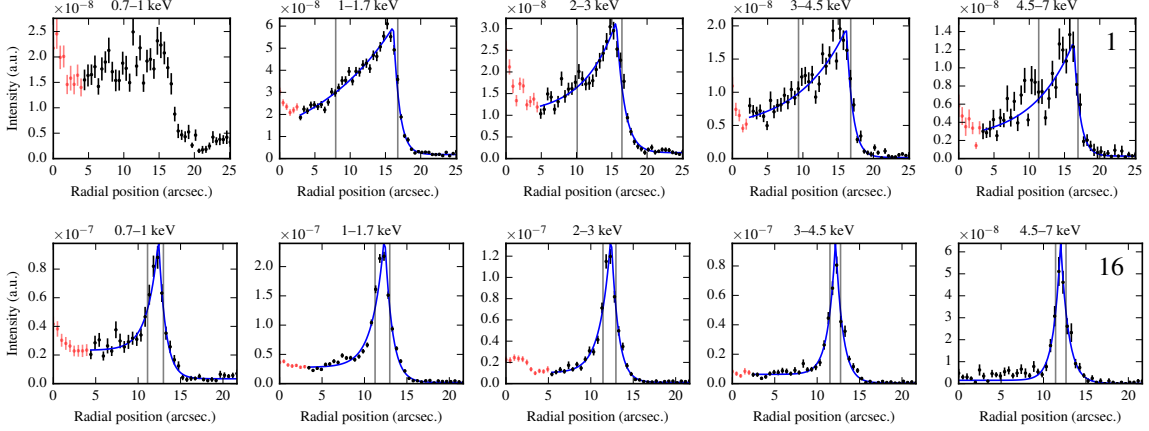


Figure 4. Best fit profiles with measured FWHMs demarcated for each energy band in Region 1 (top) and Region 16 (bottom). Hereafter, we use Regions 1 and 16 to illustrate results for profiles of differing quality and absolute width. We could not measure a 0.7–1 keV FWHM in Region 1, reflected in Table 2. Data in red were excluded from profile fit domains as described in text.

point between discrete energy bands as:

$$m_E(E_2) = \frac{\ln(w_2/w_1)}{\ln(E_2/E_1)} \quad (13)$$

where w_1, w_2 and E_1, E_2 are FWHMs and lower energy values for each energy band – e.g., m_E at 1 keV is computed using FWHMs from 0.7–1 keV and 1–1.7 keV, with $E_2 = 1$ keV and $E_1 = 0.7$ keV. Errors on m_E are propagated in quadrature from adjacent FWHM measurements.

Although the measurement scatter is quite large, shown dramatically in the point-wise computed m_E values, the mean rim width decreases consistently with increasing energy. Furthermore, mean m_E values are consistently negative and tend smoothly towards 0 (weaker energy-dependence) with increasing energy. Errors on FWHM measurements are typically $\lesssim 10\%$, reflecting the high quality of the underlying *Chandra* data. Scatter in FWHM measurements may be attributed in part to (1) our measurement procedure, which depends on an empirical choice of profile fit function, and (2) variation in Tycho's rim morphology (e.g., Figure 4).

4.2. Model fit results

Best fit results for loss-limited and damped cases are summarized in Figure 5 and Table 3 with $\mu = 1$ and $\eta_2 = 1$ both fixed. In all tables, we report values of χ^2 rather than χ^2_{red} to ease comparison of different fits, as we often manually stepped parameters that were held constant in fitting.

Table 4 reports model fits with η_2 fixed to values derived from *srcut* spectrum fits for ν_{cut} and hence η_2 from equation (8), with B_0 varying freely; cutoff-derived η_2 values of ~ 10 require increased magnetic fields compared to the $\eta_2 = 1$ case if rims are purely loss-limited. We derive different η_2 values for varying μ and find that fitted B_0 varies only weakly with μ ; for example, Regions 1 and 16 have best fit values of B_0 increasing over 252–266 μG and 660–700 μG respectively as μ ranges between 0–2, for loss-limited fits.

Magnetically damped rims are able to fit width-energy dependence in our measurements at least as well as purely loss-limited rims for an acceptable range of a_b values. As loss-limited models are a subset of damping

models, this is expected. But fits with damping lengths small enough to exert influence on rim widths are also permissible. In both loss-limited and damped fits, we do not observe systematic variation of fit parameters with azimuth around the remnant.

4.3. Fitting parameter degeneracy

We briefly explore the effects of varying η_2 and other fit parameters, before focusing on results with $\mu = \eta_2 = 1$ for simplicity. Fixing η_2 from measured ν_{cut} values does not yield any obvious insight. But, diffusion coefficients computed in this manner may give more credible derived estimates of B_0 if the DSA assumptions invoked are accurate.

Loss-limited model values of B_0 and η_2 may covary without strongly altering fit quality in many regions. If diffusion is the primary control on rim width – i.e., $l_{\text{diff}} > l_{\text{ad}}$ – then η_2 and B_0 become degenerate as the product $\eta_2^{1/2} B_0^{-3/2}$ exerts most control on rim width $w \sim l_{\text{diff}}$ (equation (11)). If advection is the primary control on rim width (widths narrow rapidly with energy; i.e., $m_E \sim -0.5$), then $\eta_2 \ll 1$ becomes unimportant and fits are well-behaved with effectively one free parameter.

We also performed loss-limited model fits with μ fixed between 0 and 2 and both η_2 and B_0 free. Fits with $\mu \lesssim 1$ generally yield larger parameter values and errors for both η_2 and B_0 , and they are more likely to be ill-constrained (e.g., $\eta_2 > 10^3$ or $B_0 > 10^3 \mu\text{G}$). Fits to the same data with varying μ can yield η_2 varying by 1–2 orders of magnitude. The χ^2 values for individual fits are variable and large ($\gg 1$), so we cannot favor or disfavor particular values of μ and η_2 . But, neglecting the magnitude of our χ^2 values, values of $\mu \geq 1$ are qualitatively favored by χ^2 in most regions. This trend may be partially an artifact of the correlation between B_0 and η_2 as they are not entirely independent parameters, but they are less correlated for larger μ ; fits at smaller μ may have fewer (non-integer) degrees of freedom, partially offsetting our observations.

Damping modifies the degeneracy in B_0 and η_2 . For small values of a_b (strong damping), increased diffusion (η_2) can cause rim widths at all energies to narrow counterintuitively. Speculatively, spatial variation of the diffusion coefficient may oppose downstream advection

Table 2
Measured full widths at half max (FWHMs) for all regions.

Region	FWHM (arcsec)					m_E (-)			
	Band 1 (0.7–1 keV)	Band 2 (1–1.7 keV)	Band 3 (2–3 keV)	Band 4 (3–4.5 keV)	Band 5 (4.5–7 keV)	Bands 1–2 (1 keV)	Bands 2–3 (2 keV)	Bands 3–4 (3 keV)	Bands 4–5 (4.5 keV)
1		$8.80^{+0.18}_{-0.15}$	$6.34^{+0.26}_{-0.21}$	$7.40^{+0.30}_{-0.23}$	$5.57^{+0.47}_{-0.42}$		-0.47 ± 0.06	0.38 ± 0.13	-0.70 ± 0.22
2		$4.22^{+0.12}_{-0.09}$	$2.36^{+0.12}_{-0.09}$	$3.00^{+0.16}_{-0.12}$	$4.11^{+0.34}_{-0.30}$		-0.84 ± 0.08	0.59 ± 0.16	0.77 ± 0.23
3		$2.47^{+0.08}_{-0.07}$	$1.78^{+0.09}_{-0.07}$	$2.10^{+0.11}_{-0.11}$	$1.32^{+0.10}_{-0.09}$		-0.47 ± 0.08	0.41 ± 0.17	-1.15 ± 0.22
4	$5.85^{+0.37}_{-0.33}$	$4.35^{+0.09}_{-0.08}$	$3.26^{+0.11}_{-0.09}$	$3.69^{+0.12}_{-0.11}$	$3.20^{+0.21}_{-0.18}$	-0.83 ± 0.18	-0.41 ± 0.05	0.31 ± 0.11	-0.35 ± 0.17
5		$4.52^{+0.11}_{-0.12}$	$3.06^{+0.11}_{-0.11}$	$3.25^{+0.15}_{-0.13}$	$3.04^{+0.21}_{-0.18}$		-0.56 ± 0.06	0.15 ± 0.14	-0.17 ± 0.19
6	$2.48^{+0.18}_{-0.18}$	$2.32^{+0.05}_{-0.06}$	$2.98^{+0.11}_{-0.09}$	$2.05^{+0.08}_{-0.09}$	$2.21^{+0.15}_{-0.14}$	-0.19 ± 0.21	0.36 ± 0.06	-0.92 ± 0.13	0.18 ± 0.19
7	$2.69^{+0.20}_{-0.17}$	$2.33^{+0.05}_{-0.05}$	$2.31^{+0.08}_{-0.08}$	$1.81^{+0.09}_{-0.07}$	$1.83^{+0.11}_{-0.08}$	-0.39 ± 0.20	-0.01 ± 0.06	-0.60 ± 0.14	0.02 ± 0.17
8	$2.33^{+0.21}_{-0.20}$	$2.72^{+0.07}_{-0.08}$	$2.38^{+0.10}_{-0.09}$	$2.10^{+0.10}_{-0.09}$	$2.37^{+0.20}_{-0.17}$	0.43 ± 0.26	-0.19 ± 0.07	-0.30 ± 0.15	0.29 ± 0.22
9	$2.16^{+0.24}_{-0.23}$	$2.35^{+0.07}_{-0.06}$	$2.47^{+0.11}_{-0.11}$	$1.91^{+0.09}_{-0.09}$	$2.20^{+0.17}_{-0.16}$	0.24 ± 0.31	0.07 ± 0.07	-0.63 ± 0.16	0.34 ± 0.22
10	$2.38^{+0.24}_{-0.23}$	$1.99^{+0.07}_{-0.06}$	$1.76^{+0.09}_{-0.08}$	$1.59^{+0.09}_{-0.08}$	$1.58^{+0.13}_{-0.12}$	-0.50 ± 0.29	-0.18 ± 0.08	-0.24 ± 0.18	-0.02 ± 0.23
11		$3.23^{+0.15}_{-0.13}$	$2.52^{+0.16}_{-0.13}$	$1.90^{+0.14}_{-0.13}$	$3.09^{+0.45}_{-0.38}$		-0.36 ± 0.10	-0.70 ± 0.22	1.21 ± 0.37
12		$3.86^{+0.17}_{-0.16}$	$2.61^{+0.15}_{-0.13}$	$3.02^{+0.22}_{-0.21}$	$2.23^{+0.21}_{-0.17}$		-0.56 ± 0.10	0.36 ± 0.22	-0.74 ± 0.27
13	$2.85^{+0.22}_{-0.17}$	$2.43^{+0.05}_{-0.05}$	$2.36^{+0.08}_{-0.05}$	$1.95^{+0.09}_{-0.10}$	$1.84^{+0.11}_{-0.14}$	-0.45 ± 0.20	-0.04 ± 0.05	-0.47 ± 0.13	-0.15 ± 0.20
14	$2.86^{+0.17}_{-0.16}$	$2.42^{+0.06}_{-0.04}$	$2.23^{+0.08}_{-0.07}$	$2.38^{+0.10}_{-0.08}$	$2.19^{+0.12}_{-0.10}$	-0.47 ± 0.17	-0.12 ± 0.06	0.17 ± 0.12	-0.20 ± 0.15
15	$2.71^{+0.17}_{-0.16}$	$1.99^{+0.05}_{-0.04}$	$1.80^{+0.06}_{-0.05}$	$1.87^{+0.07}_{-0.05}$	$1.52^{+0.09}_{-0.08}$	-0.85 ± 0.18	-0.15 ± 0.05	0.09 ± 0.11	-0.51 ± 0.16
16	$1.87^{+0.14}_{-0.13}$	$1.73^{+0.04}_{-0.03}$	$1.52^{+0.06}_{-0.05}$	$1.25^{+0.06}_{-0.04}$	$1.23^{+0.08}_{-0.06}$	-0.22 ± 0.21	-0.18 ± 0.06	-0.49 ± 0.13	-0.04 ± 0.17
17	$1.65^{+0.13}_{-0.12}$	$1.92^{+0.05}_{-0.05}$	$1.54^{+0.06}_{-0.07}$	$1.45^{+0.07}_{-0.06}$	$2.05^{+0.16}_{-0.14}$	0.43 ± 0.22	-0.31 ± 0.07	-0.16 ± 0.15	0.86 ± 0.21
18		$4.45^{+0.13}_{-0.12}$	$3.18^{+0.17}_{-0.16}$	$2.96^{+0.20}_{-0.19}$	$1.65^{+0.21}_{-0.16}$		-0.49 ± 0.09	-0.17 ± 0.21	-1.45 ± 0.32
19		$2.30^{+0.08}_{-0.06}$	$2.28^{+0.11}_{-0.08}$	$2.16^{+0.12}_{-0.11}$	$1.60^{+0.17}_{-0.14}$		-0.02 ± 0.08	-0.13 ± 0.17	-0.74 ± 0.27
20	$4.81^{+0.31}_{-0.31}$	$1.84^{+0.06}_{-0.03}$	$1.87^{+0.08}_{-0.06}$	$1.56^{+0.07}_{-0.06}$	$2.14^{+0.23}_{-0.23}$	-2.68 ± 0.19	0.02 ± 0.07	-0.44 ± 0.14	0.77 ± 0.28
Mean	2.89 ± 0.35	3.11 ± 0.37	2.53 ± 0.23	2.47 ± 0.30	2.35 ± 0.23	-0.46 ± 0.24	-0.25 ± 0.06	-0.14 ± 0.10	-0.09 ± 0.15

Note. — Mean values computed for all regions; mean m_E values are averages for region m_E values (i.e., not computed from mean FWHMs). Errors on mean values are standard errors of the mean. Horizontal rules group individual regions into filaments.

Table 3
Best width-energy fit parameters, $\mu = \eta_2 = 1$

Region	Loss-limited		Damped		a_b
	B_0 (μG)	χ^2	B_0 (μG)	χ^2	
1	182	35.1	28	24.3	0.008
2	312	80.9	25	74.4	0.003
3	426	21.5	27	23.9	0.002
4	284	50.9	28	29.9	0.004
5	288	19.3	25	14.5	0.003
6	410	173.7	68	65.2	0.004
7	418	50.9	291	11.6	0.006
8	388	47.7	138	10.0	0.005
9	414	65.1	78	14.2	0.004
10	466	17.1	29	1.5	0.002
11	355	12.0	317	15.6	0.010
12	317	9.6	26	10.4	0.003
13	400	52.7	258	10.4	0.006
14	383	102.9	60	12.7	0.004
15	431	70.3	48	20.0	0.003
16	493	15.0	434	4.0	0.006
17	467	61.6	232	29.0	0.004
18	283	28.1	24	27.5	0.003
19	401	36.9	78	8.3	0.004
20	463	121.8	58	93.8	0.003

Note. — Fits for Regions 1–3, 5, 11, 12, 18, and 19 have 3 degrees of freedom; all others have 4. The choice of a best a_b value may be construed as removing one additional dof. Damped fits require a_b to be smaller than the FWHM at 2 keV in order to rule out effectively loss-limited fits with large a_b .

Table 4
Best model fits for all regions, η_2 derived from `srcut` fits, $\mu = 1$

Region	η_2	Loss-limited		Damped		a_b
		B_0 (μG)	χ^2	B_0 (μG)	χ^2	
1	12.0	256	29.1	19	25.5	0.008
2	11.8	443	99.4	18	72.0	0.003
3	10.6	599	31.8	19	29.3	0.002
4	12.0	402	36.2	19	34.5	0.004
5	12.9	419	32.5	19	19.1	0.004
6	11.9	568	89.7	147	61.9	0.006
7	15.3	617	11.7	473	11.1	0.009
8	8.4	511	15.1	333	10.0	0.008
9	11.2	573	23.3	66	13.7	0.005
10	9.4	631	1.4	478	2.0	0.007
11	6.1	452	18.1	21	17.5	0.003
12	3.7	375	12.6	21	9.7	0.003
13	8.4	529	13.8	368	9.9	0.008
14	11.9	547	28.6	120	12.4	0.006
15	9.5	598	23.1	426	20.0	0.007
16	8.4	670	6.3	22	5.8	0.002
17	9.0	637	32.6	32	29.4	0.003
18	14.6	432	72.4	17	16.6	0.003
19	8.9	542	12.8	209	7.7	0.006
20	9.6	631	96.0	29	94.2	0.003

Note. — η_2 values are computed from equation (8) and held fixed in model fits. All comments for Table 3 apply to `srcut` fits as well.

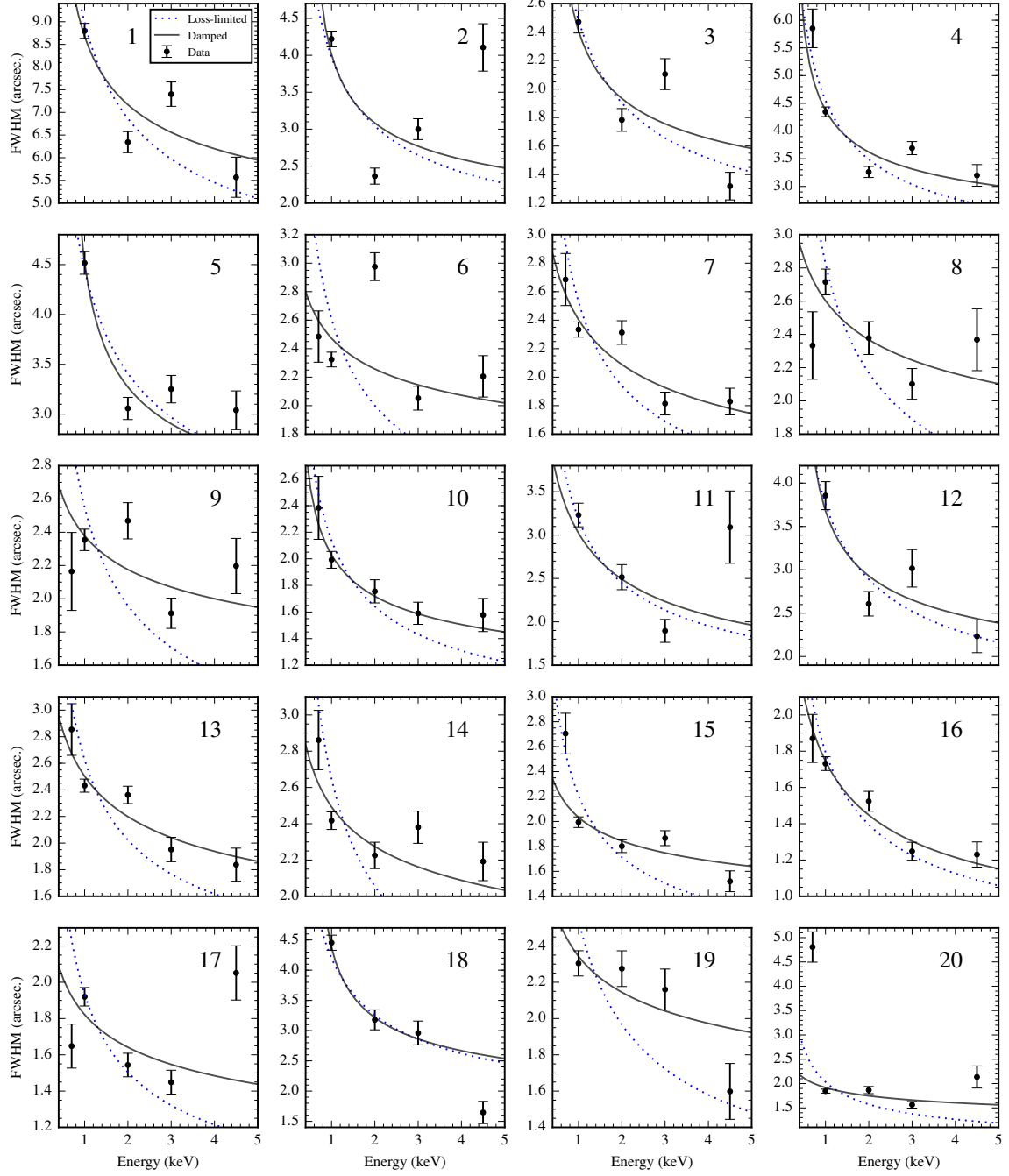


Figure 5. Rim width fits as a function of energy for loss-limited and damped fits with $\mu = 1$ and $\eta_2 = 1$ fixed for all regions, from best fit parameters in Table 3. Damped model predictions (e.g., Region 5) are not given at low energies if FWHMs cannot be calculated for model profiles (i.e., modeled intensity behind thin rim exceeds half-maximum of rim peak within model domain of $\sim 20''$). Ordinate (y) axis limits vary between subplots and are offset from the origin to better show model predictions and data variation.

through a decreased effective velocity $v_d - (\partial D / \partial x)$ in our transport equation:

$$\left[v_d - \frac{\partial D(x)}{\partial x} \right] \frac{\partial f}{\partial x} - D(x) \frac{\partial^2 f}{\partial x^2} - \frac{\partial}{\partial E} (b B^2 E^2 f) = K_0 E^{-s} e^{-E/E_{\text{cut}}} \delta(x), \quad (14)$$

requiring thinner rims as η_2 and hence $\partial D(x) / \partial x$ increase. Moreover, the effective velocity may impact rim widths even if advection dominated. In practice, if η_2

varies freely in damped fits, we observe that smaller values of a_b permit and favor smaller best fit values of both B_0 and η_2 .

Best fit B_0 values are smallest for η_2 approaching 0 and $\mu = 2$; intuitively, $\mu > 1$ strengthens diffusion at energies > 2 keV for fixed η_2 , permitting a smaller best fit η_2 and hence smaller B_0 . Fixing $\eta_2 = 1$ (Table 3), however, ties the range of B_0 values to the range of observed rim widths. Our minimum loss-limited values of B_0 are consistent with prior estimates of ~ 200 – $300 \mu\text{G}$ for

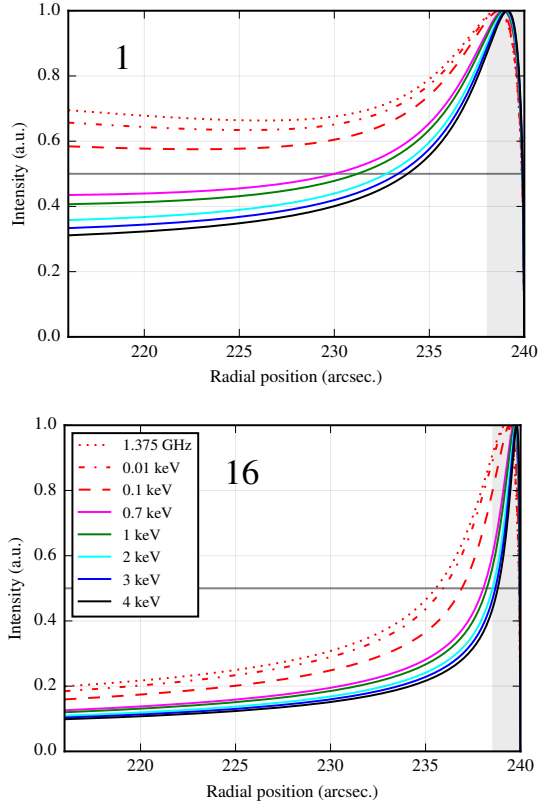


Figure 6. Model predictions illustrate weak-field (Region 1) and strong-field damping (Region 16) for damped best fit parameters with $\mu = 1$ and $\eta_2 = 1$ fixed. In X-ray energies (0.7–4.5 keV) model profiles are not strongly energy dependent, but weak-field damping profiles evolve and show no measurable FWHM at sufficiently low energies. Profiles are normalized to peak thin rim intensity, and shaded regions indicate damping lengthscale a_b . Model parameters are given in Table 3.

advection-dominated transport (Völk et al. 2005; Parizot et al. 2006; Morlino & Caprioli 2012). If loss-limited, Tycho’s rims require strong magnetic field amplification to $\sim 100\times$ typical galactic field values of $\sim 2\text{--}3\ \mu\text{G}$, versus the expected $4\times$ amplification from a strong shock.

Magnetic damping fits permit much smaller values of B_0 , as expected. The minimum value of B_0 is around $20\ \mu\text{G}$, which would require no field amplification beyond that from a strong shock. Fixing $B_{\min} = 2\ \mu\text{G}$ instead of $5\ \mu\text{G}$ permits smaller fit B_0 values, though fit values for both η_2 and B_0 still display considerable scatter.

5. DISCUSSION

5.1. Damping is poorly-constrained by X-ray width-energy dependence

Width-energy dependence is not as sensitive a discriminant between damping and loss-limited models as may be intuitively expected. Both loss-limited and damped fits do not perfectly capture sharp drop-offs (especially between 0.7–1 keV and 1–2 keV), and the data show large scatter (Figure 5). In most regions, best fit width-energy curves have $m_E \sim -0.2$. Only sharp decreases in rim width ($m_E \sim -0.5$) can disfavor damping as a control on rim widths (e.g., Region 18).

When width-energy dependence is weak, both loss-limited and damped models give best fits with similar

profiles – amplified magnetic fields in both models cause rim intensities to drop sharply. When width-energy dependence is stronger, damping profiles yield energy dependent rims if magnetic fields are small (say, $\lesssim 50\ \mu\text{G}$) and the damping lengthscale is much smaller than rim FWHMs. Figure 6 shows this contrasting behavior using best fit parameters for Regions 1 and 16.

The best damped fit parameters for Regions 1–5, 10, 12, and 18 predict a 1.375 GHz radio profile that does not drop below 50% of peak intensity within $\sim 20''$ downstream of the shock, which we treat as having no measurable FWHM. These regions are all best fit with field $B_0 < 40\ \mu\text{G}$. We refer to this model behavior as “weak-field” damping, associated with weak magnetic fields and stronger emission intensity immediately downstream of the thin rim. As observation frequency decreases, rim and trough contrast decreases, causing rim FWHMs to increase and eventually become unmeasurable. Rim width-energy dependence strengthens dramatically ($m_E \rightarrow -\infty$), permitting model fits to replicate strong width-energy dependence in observed rim widths. Weak-field fit parameters require energy losses downstream of the shock to produce energy dependence in a damped field, as discussed in Section 2.5.2.

Damping model fits to all other regions predict consistently thin rims with measurable FWHMs at decreasing energy. The width-energy dependence parameterized by m_E trends towards zero at low energy, indicating that rim widths are comparatively energy independent. At higher energy, such rims narrow slightly with increasing energy ($m_E \sim -0.2$) to match the observed width-energy dependence in X-rays. The gradual increase in $|m_E|$ with energy is expected in the damping model as advection and/or diffusion take control of rim widths at increasing energy, as discussed in Section 2.5. The best damped fits for these regions all have larger B_0 values than in the “weak-field” damping case. We refer to these fits as giving rise to “strong-field” damping, associated with stronger magnetic fields, weaker emission intensity behind the thin rim, and clear rims with measurable FWHMs at low photon energies (at and below soft X-rays).

We are unable to determine whether weak- or strong-field damping is descriptive of Tycho’s shock magnetic field, given the large χ^2 values on our model fits. Several regions may be well-fit by “weak-field” and “strong-field” damping alike. But, the qualitative behavior of B_0 is suggestive; very strong fields at the shock ($\gtrsim 100\ \mu\text{G}$) with magnetic field damping on a scale comparable to rim FWHMs appear incompatible with significant energy dependence. The distinction between weak- and strong-field damping may be equally well described as strong versus weak damping. The dichotomy reflects additional degeneracy between a_b and B_0 – for a given rim width, increased damping length a_b requires increased B_0 to reproduce the same width, and vice versa.

Although model fits are poorly-constrained, we attempt to further explore how damping and synchrotron losses set rim widths for damped fits with finite a_b . Table 5 compares rim widths at 2 keV to advection lengthscale l_{ad} and damping lengthscale a_b from the loss-limited and damped fits of Table 3. As discussed in Section 2.5, loss-limited rim widths are qualitatively set by either damping or the dominant transport process as

Table 5
Lengthscale analysis

Region	Measurements		Loss-lim. fit		Damped fit			
	v_d (10^8 cm/s)	w (2 keV) (% r_s)	l_{ad} (% r_s)	l_{ad}/l_{diff} (-)	l_{ad} (% r_s)	a_b (% r_s)	l_{ad}/a_b (-)	$w(2 \text{ keV})/a_b$ (-)
1	1.30	2.64	0.61	1.40	10.26	0.80	12.83	3.30
2	1.29	0.99	0.27	1.39	11.54	0.30	38.48	3.28
3	1.29	0.74	0.17	1.38	10.80	0.20	54.00	3.72
4	1.28	1.36	0.31	1.38	10.08	0.40	25.20	3.40
5	1.28	1.27	0.30	1.37	12.07	0.30	40.24	4.25
6	1.28	1.24	0.18	1.37	2.61	0.40	6.53	3.10
7	1.27	0.96	0.17	1.36	0.29	0.60	0.49	1.61
8	1.27	0.99	0.19	1.36	0.90	0.50	1.80	1.98
9	1.26	1.03	0.17	1.36	2.09	0.40	5.23	2.57
10	1.26	0.73	0.14	1.35	9.21	0.20	46.05	3.66
11	1.25	1.05	0.21	1.34	0.25	1.00	0.25	1.05
12	1.24	1.09	0.25	1.33	10.80	0.30	35.98	3.62
13	1.23	0.98	0.18	1.32	0.34	0.60	0.57	1.64
14	1.14	0.93	0.17	1.23	2.84	0.40	7.10	2.32
15	1.14	0.75	0.15	1.22	3.95	0.30	13.16	2.50
16	1.13	0.63	0.12	1.21	0.14	0.60	0.24	1.06
17	1.12	0.64	0.13	1.20	0.36	0.40	0.91	1.61
18	1.15	1.32	0.28	1.23	11.29	0.30	37.64	4.42
19	1.18	0.95	0.17	1.27	1.99	0.40	4.97	2.37
20	1.17	0.78	0.14	1.26	3.08	0.30	10.28	2.59

Note. — All lengthscales computed at fiducial energy 2 keV from best fits with $\eta_2 = 1$ and $\mu = 1$. Ratio of l_{ad}/l_{diff} is same for loss-limited and damped fits and depends only on plasma velocity v_d and observation energy, as l_{ad}/l_{diff} is independent of B_0 for $\mu = 1$.

$w \sim \min(a_b, \max(l_{ad}, l_{diff}))$. At 2 keV with $\eta_2 = 1$ and $\mu = 1$ fixed, the ratio l_{ad}/l_{diff} is nearly constant; variation (1.2–1.4) arises solely from azimuthal variation in shock velocity. If rims are loss-limited and diffusion is negligible, we anticipate rim widths $w = 4.6l_{ad}$, where the factor 4.6 may be derived assuming spherical symmetry and an exponential synchrotron emissivity (Ballet 2006). At 2 keV, we find that loss-limited rim widths $w \sim 5l_{ad}$ due to diffusion. Enforcing $w(2 \text{ keV})/a_b > 1$ for damped fits still permits $l_{ad}/a_b < 1$ as $w(2 \text{ keV}) \lesssim 5l_{ad}$, with damping decreasing $w(2 \text{ keV})$ below the expected loss-limited width at a given B_0 . We may impose a tighter or looser bound, but our results should not be greatly affected given large uncertainty in our fits and associated degeneracy between B_0 and a_b .

Our modeling can also reassess the significance of rim width-energy dependence in the remnant of SN 1006 presented by R14. We fit averaged filament widths in SN 1006 measured by R14 to our damping model using the same procedure as for Tycho. We fix $B_{min} = 5 \mu\text{G}$, although best fit magnetic fields for SN 1006 are smaller than those of Tycho due to the much wider filaments of SN 1006. A more extensive search of parameter space produces acceptable damping (hybrid) models with more rapid shrinkage than found in R14. Damped fits are comparable to or better than loss-limited fits in 3 of 5 filaments in SN 1006. Fits to two filaments with strong energy dependence ($m_E \sim -0.5$) favor a loss-limited model with sub-Bohm diffusion ($\eta_2 \ll 1$), though sub-Bohm diffusion may be an unphysical result pointing to oversimplifications in the model. The width-energy dependence in SN 1006 ($m_E \sim -0.3$ to -0.5) is overall slightly stronger than in Tycho, and the best damped fits for SN 1006 all fall into the “weak-field” case. The best fit B_0 values are less than $40 \mu\text{G}$ in the damped model, compared to ~ 100 – $200 \mu\text{G}$ in the loss-limited model. If thin radio rims in SN 1006 (Reynolds & Gilmore 1986) indi-

cate magnetic field damping on lengthscales comparable to X-ray filament widths, some magnetic damping is not incompatible with rim width narrowing. A future study of SN 1006 with recent multi-frequency Karl G. Jansky Very Large Array data (PI: D. Green) may verify whether radio and X-ray rims can be jointly described by an amplified and subsequently damped magnetic field.

5.2. Model assumptions and correctness

Our models adopted a distance d to Tycho of 3 kpc, but estimates for Tycho’s distance range between 2.3–4 kpc (Hayato et al. 2010). As a larger remnant distance would increase both physical filament widths and shock velocity estimates from proper motion, we may derive expected scalings for modeled η_2 and B_0 as functions of assumed distance d . The advective lengthscale, equation (10), may be rearranged to obtain:

$$B_0 = (3.17 \mu\text{G}) \left(\frac{v_d}{10^8 \text{ cm/s}} \right)^{2/3} \times \left(\frac{l_{ad}}{0.01 \text{ kpc}} \right)^{-2/3} \left(\frac{h\nu}{1 \text{ keV}} \right)^{-1/3} \quad (15)$$

or, more simply,

$$B_0 \propto (v_d)^{2/3} (l_{ad})^{-2/3} \nu^{-1/3}. \quad (16)$$

Both l_{ad} and v_d scale linearly with remnant distance d and thus their effects cancel in determining the magnetic field. If diffusion is the primary control on filament lengthscales, equation (11) yields:

$$\eta_2 \propto (l_{diff})^2 B_0^{(\mu+5)/2} \nu^{-(\mu-1)/2} \quad (17)$$

Model fits with varying distance obey both scalings, $\eta_2 \propto d^2$ and B_0 constant. When comparing model fits with remnant distances of 3 kpc and 4 kpc, the deviation from the idealized scaling is $\lesssim 1\%$ for B_0 and ~ 1 –

5% for η_2 . As varying remnant distance d leaves width-energy scaling m_E invariant, the relative contributions of l_{ad} and l_{diff} should also be invariant. Then both length-scales should scale simultaneously with d , yielding the observed behavior. In the damped model, a larger distance d will require larger physical damping lengths from magnetic turbulence. But, fitted values of a_b should remain unchanged as we report a_b in units of shock radius r_s .

The exponential variation in $D(x)$ (equation (6)) may not be physically reasonable; as noted above, the assumption $D(x) \propto 1/B^2(x)$ gives rise to sharp gradients in diffusion coefficient and even inverts the effect of η_2 on our model profiles (where larger η_2 can cause rim widths to narrow). Nevertheless, the modeled behavior appears physically reasonable. Only X-ray profiles are impacted by the assumption on $D(x)$ as radio profiles assume no diffusion. And, model behavior driven by advection and magnetic damping – namely, rim width-energy dependence in a damped magnetic field – occurs for $D = 0$, and cannot be an artifact of our assumption that $D(x)B^2(x)$ is constant.

We emphasize that additional counts from averaging measurements or selecting larger regions will likely not improve our ability to constrain B_0 and η_2 from width-energy modeling. This is easily seen from Figure 5 as well as large χ^2 values in Tables 3 that reflect relatively tight errors in our FWHM profile measurements (Table 2).

5.3. Other potential constraints

Rim width-energy dependence is a morphological manifestation of spectral softening downstream of the forward shock; previously, Cassam-Chenaï et al. (2007) also sought to distinguish loss-limited and damped rims with a careful spectral study and 1-D hydrodynamical model. Although knowledge of radial spectral variation, in principle, fully determines rim profiles, there is not a clear relationship between observed spectral variation and rim widths alone. Our model, for example, replicates observed rim width variation but underpredicts the observed spectral variation. The more sophisticated model of Cassam-Chenaï et al. (2007) similarly has trouble reproducing the observed radial gradient in spectral photon index. Photon indices predicted in our model, for integrated model rim spectra similar to those of Figure 3 and Table 1, are also somewhat ill-constrained. Enforcing limits on acceptable model photon indices (e.g., Fig. 16 Cassam-Chenaï et al. 2007) could help constrain shock parameters or identify discrepancies between model assumptions and measurements.

Estimates of magnetic field strength that depend upon global models for Tycho’s evolution (e.g., Morlino & Caprioli 2012) may not help constrain our rim model results. In such models, assumptions on particle acceleration and magnetic field evolution downstream of the shock (e.g., further damping or amplification at the reverse shock and contact discontinuity) would affect the spatially integrated spectrum of Tycho. We have focused on effects immediately behind the forward shock, making as few assumptions as possible about particle acceleration and magnetic fields throughout the remnant. It may not make sense to extrapolate our results to estimate magnetic fields throughout the remnant or, similarly, to use global models to constrain our results given all as-

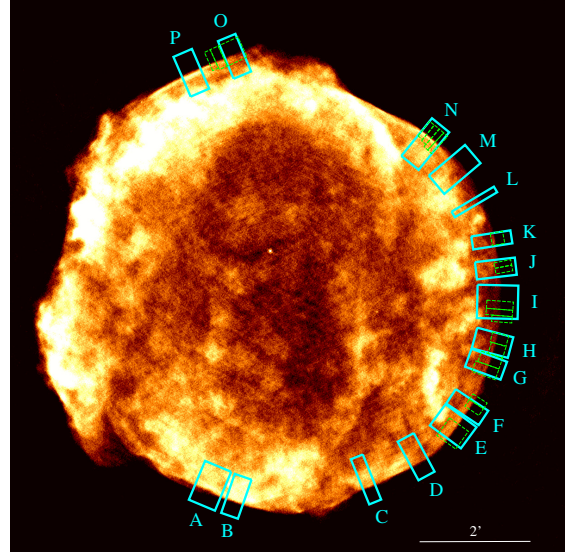


Figure 7. Radio image of Tycho’s SNR at 1.375 GHz with linear scaling. Extraction regions (green) for joint radio and X-ray profile analysis overlay region selections for X-ray rim width analysis (Figure 1).

sumptions involved.

6. JOINT RADIO AND X-RAY MODELING

Thin radio rims spatially coincident with X-ray synchrotron rims may help constrain magnetic field damping. Radio synchrotron emission in the remnant interior may arise from not only recently shock-accelerated electrons but also long-lived electrons interacting with a turbulent field inside the remnant, as \sim GeV electrons have cooling times of order 10^5 – 10^7 yr in 10–100 μ G magnetic fields. But simple models for synchrotron emissivity as a function of density in Sedov and pre-Sedov dynamical stages predict radio synchrotron profiles rising gradually to broad maxima well inside the shock radius (e.g. Reynolds & Chevalier 1981; Reynolds 1988). Our steady-state planar transport model predicts monotonically increasing emission downstream of the forward shock in a loss-limited model, until sphericity becomes important and our model is inapplicable. On scales of a few percent of the remnant radius, only magnetic field damping can cause emission to decrease.

The idea of modeling X-ray and radio profiles jointly was pioneered by Cassam-Chenaï et al. (2007), who found that sharp radio rims in Tycho were not reproduced by a loss-limited model. Cassam-Chenaï et al. (2007) considered loss-limited and damping profiles consistent with physical constraints applied in a hydrodynamical model. Here, we neglect physical constraints and estimate a damping length necessary to generate radio rims with shape similar to observations.

We extract radio profiles from a 1.375 GHz image of Tycho taken with the Very Large Array (VLA) in A configuration in March 1994 (PI: D. Moffett); see Reynoso et al. (1997) for a detailed presentation. The half-power beam width of $\sim 1.5''$ just resolves thin radio rims and structure near the forward shock; the image is sampled at $0.5''$. We also extracted 4–7 keV X-ray profiles in all regions from the previous archival *Chandra* observation to jointly model radio and X-ray profiles, permit-

Table 6
Fit parameters from profile shape comparison

Region	B_0 (μG)	a_b (-)	Region	B_0 (μG)	a_b (-)
A	50	0.020	I	250	0.020
B	200	0.050	J	300	∞
C	15	0.010	K	400	0.010
D	100	0.050	L	250	∞
E	120	0.030	M	200	∞
F	300	0.025	N	800	0.010
G	250	0.020	O	200	0.005
H	300	0.020	P	150	0.012

Note. — Damping lengths of ∞ indicate that a loss-limited fit is favored ($a_b > 10\%$ of shock radius r_s).

ting somewhat firmer discrimination of plausible model parameters. Figure 7 shows the extraction regions overlaying the radio image and the previous X-ray profile regions of Figure 1.

We compute model radio and X-ray measured profiles from the transport model of equation (1) for varying B_0 and a_b , similar to those shown in Figure 2. The parameters $B_{\min} = 5 \mu\text{G}$, $\eta_2 = 1$, and $\mu = 1$ are held fixed. Diffusion, in particular, is negligible for modeled radio emission as particle energies are 3 orders of magnitude lower than in X-ray. Neglecting diffusion also circumvents the unphysical assumption that $D(x)B^2(x)$ is constant, which was invoked to obtain Green's function solutions to equation (1).

We align each set of model profiles at some B_0 and a_b to measurements by eye, varying relative amplitudes and translations in radio and X-ray independently to best match the measured profiles. Although “fitting” by eye does not quantitatively bound model parameters, we can find plausible values of B_0 and a_b and estimate the importance of magnetic damping throughout the remnant. More involved nonlinear fitting may be unreliable as we cannot constrain spatially heterogeneous radio emission within the remnant. Moreover, our transport model neglects self-similar downstream evolution of shocked plasma (decaying velocity, density, and magnetic field) and is inaccurate further downstream than $\sim 10\%$ of the shock radius.

The joint radio and X-ray profile modeling contrasts strongly with our previous width-energy fitting from X-ray measurements alone, which neglected profile shape in favor of more robust FWHM measurements. Manually fitting profiles allows us to consider radio and X-ray filaments that do not have well-defined FWHMs, especially as radio rims do not fall below 50% of the peak emission. We can also use profiles from regions not previously considered due to the lack of an X-ray FWHM, especially in softer (0.7–4 keV) X-rays.

We identify three classes of radio profiles: thin rims with downstream troughs, plateaus, and continuous rises. Regions B, C, and D (southern limb) show plateaus in radio emission. Regions J, L, and M (around NW) show continuous rises in emission. All other regions have a radio rim within $15''$ of the forward shock, where the forward shock in radio is assumed at zero intensity. Figure 8 shows extracted radio and nonthermal X-ray (4–7 keV) profiles for three well-fit regions with our best manually selected model profiles, illustrating each of the three radio profile types observed.

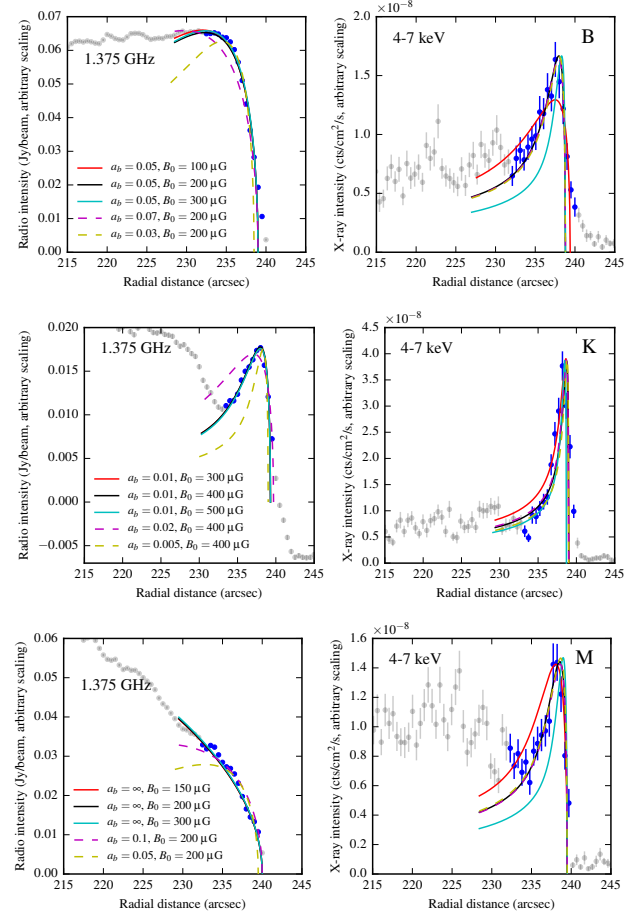


Figure 8. Measured radio and X-ray profiles plotted with model profiles for varying a_b and B_0 in each region, showing typical parameters (and ranges) required to reproduce radio and X-ray rims simultaneously in our model. *Solid black curves* in all regions plot our manually chosen best model profiles. Profiles are chosen to show varying radio rim morphology, including plateaus (B), thin rims with troughs (K), and continuous rises (M); these profiles show some of the best agreement of our selected regions, but cf. Figure 9. Profile radial coordinates are shifted arbitrarily to aid visual comparison. Negative radio intensity is unphysical and associated with deconvolution of raw VLA visibilities.

Our model requires damping length $a_b \lesssim 0.1$ to produce a plateau or thin rim in radio emission. For regions with thin radio rims, the best manually selected profiles have B_0 between 50–400 μG , neglecting only Region N which could not be modeled simultaneously in both X-ray and radio (Figure 9). The damping length a_b ranges between 0.01–0.03, or 2–7 $''$. We list estimated best fit parameters in Table 6.

The radio plateaus in regions B, C, D are compatible with damping lengths between 0.01–0.05. Continuous rises in radio emission are best modeled with $a_b \gtrsim 0.1$ and $B_0 \sim 200$ –300 μG . Although damping lengths $a_b \gtrsim 0.1$ are not physically meaningful well beyond the shock, these large values of a_b yield practically constant magnetic field near the shock. Our results are also insensitive to the assumed value of B_{\min} ; only model profiles with small magnetic fields ($B_0 \lesssim 100 \mu\text{G}$) and/or small damping length ($a_b < 0.01$) are affected if we take $B_{\min} = 2 \mu\text{G}$ rather than 5 μG .

Tycho's shock structure is more complex than assumed

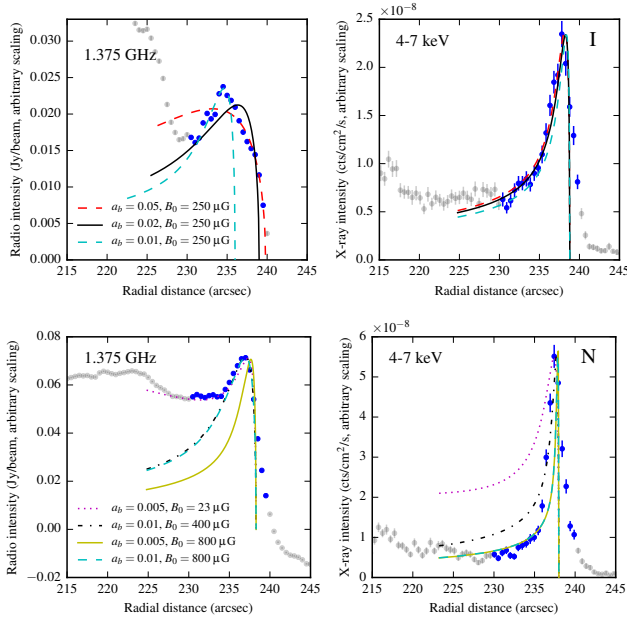


Figure 9. Extracted profiles poorly reproduced by our model, compared to Figure 8. Region I shows irregularly shaped radio rim. Region N contains two superposed filaments that cannot be modeled by a single rim in both X-ray and radio; the narrow X-ray rim requires atypically strong magnetic fields ($\sim 800 \mu\text{G}$), and the emission plateau behind the radio rim requires small damping lengths ($a_b \sim 0.005$).

by our transport model. Emission towards the remnant interior clearly shows spatial structure (Figure 7). Figure 9 shows two regions that were poorly described by our model. A majority of our regions have irregular rims; in at least 2–3 regions, this may be attributed to projection of multiple filaments. Others (e.g., Region K) show rims with slopes that cannot be matched by our models, whether too steep or shallow. Shape mismatch may be attributed in part to point-spread mismatch, diffusion (e.g., $\eta_2 \neq 1$), shock precursors, or other effects. Nevertheless, the conclusion that thin radio rims require magnetic damping is supported by more sophisticated modeling. As we have noted, hydrodynamic models with diffusive shock acceleration (Cassam-Chenaï et al. 2007; Slane et al. 2014) also cannot produce radio profiles with narrow rims in a purely advected magnetic field. It is also not clear that radio structure is due to a global radial variation in magnetic field strength. E.g., Slane et al. (2014) suggest that Rayleigh-Taylor fingers between the forward shock and contact discontinuity could locally confine radio-emitting electrons, creating observed radio rim structure. But, if radio rims are due strictly to magnetic field effects, our conclusions on magnetic field drop-off are independent of the causative physical mechanism so long as they yield magnetic field fall-off over 1% of remnant radius.

We may also use spatially overlapping radio and X-ray region selections (Figure 7) to attempt to constrain X-ray width-energy fits. All X-ray region selections (Figure 1) are associated with radio rims, except for Regions 11 and 12 underlying Region J in radio. X-ray emission at regions B, C, D (radio plateaus) and L, M (radio rises) showed rims, but their widths either could not be measured, or could only be measured in the 4–7 keV band.

If radio rims require damping at $\sim 1\%$ remnant radius, width-energy fits with “weak-field” damping lengthscales of $\sim 0.5\%$ may be disfavored. Conversely, the radio and X-ray filament of Regions 11, 12 and J is the best remaining loss-limited rim candidate, although width-energy fits are equivocal towards damped and loss-limited models.

7. CONCLUSIONS

We measured the widths of several thin synchrotron filaments around Tycho’s supernova remnant and found moderate narrowing of rim widths throughout the remnant, corroborating rim narrowing observed by Ressler et al. (2014) in the remnant of SN 1006. We confirmed that selected filaments are dominated by nonthermal emission and have clearly measurable full widths at half maximum in 4–5 energy bands. Both X-ray width-energy fits and joint radio/X-ray profile modeling require magnetic fields $\gtrsim 20 \mu\text{G}$ even with magnetic damping.

A steady-state particle transport model with constant magnetic field gives diffusion coefficients and magnetic field strengths broadly consistent with prior estimates from rim widths (e.g., Parizot et al. 2006; Rettig & Pohl 2012) and radio and gamma ray measurements (Acciari et al. 2011; Morlino & Caprioli 2012). The same model with a damped magnetic field is equally capable of describing our measured data. At weak energy dependence the two models are indistinguishable and magnetic damping fits favor moderately amplified magnetic fields beyond simple compression, but lower than for loss-limited models. At moderate energy dependence ($m_E \sim -0.3$), the damping model permits weak magnetic fields and short damping lengths ($< 1\%$ remnant radius) to reproduce energy dependence, but we still cannot favor either damped or loss-limited rims due to fit uncertainty. The distinction between loss-limited and damped models is somewhat artificial; only for large differences between the various transport lengthscales, a frequency-dependent occurrence, is one or the other mechanism clearly dominant.

Thin radio synchrotron rims, however, are not reproduced in loss-limited models (Cassam-Chenaï et al. 2007). Assuming shocked electrons account for most radio emission immediately downstream of Tycho’s forward shock, we jointly model radio and X-ray profiles and find that damping lengths of 1–5% of the shock radius are required throughout most of the remnant; only a few (3/16) selected regions are plausibly consistent with a constant advected magnetic field. Typical magnetic field strengths range between 50–400 μG . Although we cannot bound damping lengths and fields from our qualitative profile comparisons, our results are physically reasonable and are likely good to order-of-magnitude. If damping lengths inferred from radio rims are correct, “weak-field” damping is disfavored in explaining X-ray rim width-energy dependence, and damped rims require magnetic field amplification to $\sim 100 \mu\text{G}$ or more in Tycho.

We thank the anonymous referee for comments that helped clarify and improve the manuscript. David Moffett kindly provided the VLA image used in this study. The scientific results reported in this article are based on data obtained from the *Chandra* Data Archive. This

research made extensive use of NASA's Astrophysics Data System. This research also made use of APLpy, an open-source plotting package for Python hosted at <http://aplpy.github.com>.

Facilities: CXO (ACIS-I), VLA

REFERENCES

- Acciari, V. A., Aliu, E., Arlen, T., et al. 2011, *ApJ*, 730, L20
- Acero, F., Aharonian, F., Akhperjanian, A. G., et al. 2010, *A&A*, 516, A62
- Ackermann, M., Ajello, M., Allafort, A., et al. 2013, *Science*, 339, 807
- Aharonian, F. A., Akhperjanian, A. G., Aye, K.-M., et al. 2004, *Nature*, 432, 75
- Ballet, J. 2006, *Advances in Space Research*, 37, 1902
- Bamba, A., Yamazaki, R., Ueno, M., & Koyama, K. 2003, *ApJ*, 589, 827
- Bamba, A., Yamazaki, R., Yoshida, T., Terasawa, T., & Koyama, K. 2005, *ApJ*, 621, 793
- Berezhko, E. G., & Völk, H. J. 2004, *A&A*, 419, L27
- Bykov, A. M., Ellison, D. C., Osipov, S. M., & Vladimirov, A. E. 2014, *ApJ*, 789, 137
- Cassam-Chenaï, G., Hughes, J. P., Ballet, J., & Decourchelle, A. 2007, *ApJ*, 665, 315
- Chen, X., Chatterjee, R., Zhang, H., et al. 2014, *MNRAS*, 441, 2188
- Ellison, D. C., Moebius, E., & Paschmann, G. 1990, *ApJ*, 352, 376
- Eriksen, K. A., Hughes, J. P., Badenes, C., et al. 2011, *ApJ*, 728, L28
- Ferrand, G., Danos, R. J., Shalchi, A., et al. 2014, *ApJ*, 792, 133
- Green, D. A. 2014, *Bulletin of the Astronomical Society of India*, 42, 47
- Han, J. L., Manchester, R. N., Lyne, A. G., Qiao, G. J., & van Straten, W. 2006, *ApJ*, 642, 868
- Hayato, A., Yamaguchi, H., Tamagawa, T., et al. 2010, *ApJ*, 725, 894
- Heckman, T. M., Armus, L., & Miley, G. K. 1990, *ApJS*, 74, 833
- Hwang, U., Decourchelle, A., Holt, S. S., & Petre, R. 2002, *ApJ*, 581, 1101
- Kardashev, N. S. 1962, *Soviet Ast.*, 6, 317
- Katsuda, S., Tsunemi, H., Uchida, H., & Kimura, M. 2008, *ApJ*, 689, 225
- Lerche, I., & Schlickeiser, R. 1980, *ApJ*, 239, 1089
- Lyne, A. G., & Smith, F. G. 1989, *MNRAS*, 237, 533
- Marcowith, A., & Casse, F. 2010, *A&A*, 515, A90
- Morlino, G., Amato, E., Blasi, P., & Caprioli, D. 2010, *MNRAS*, 405, L21
- Morlino, G., & Caprioli, D. 2012, *A&A*, 538, A81
- Pacholczyk, A. G. 1970, *Radio Astrophysics* (San Francisco: W. H. Freeman)
- Parizot, E., Marcowith, A., Ballet, J., & Gallant, Y. A. 2006, *A&A*, 453, 387
- Patnaude, D. J., & Fesen, R. A. 2007, *AJ*, 133, 147
- Pohl, M., Yan, H., & Lazarian, A. 2005, *ApJ*, 626, L101
- Ressler, S. M., Katsuda, S., Reynolds, S. P., et al. 2014, *ApJ*, 790, 85
- Rettig, R., & Pohl, M. 2012, *A&A*, 545, A47
- Reville, B., & Bell, A. R. 2013, *MNRAS*, 430, 2873
- Reynolds, S. P. 1988, in *Supernova Remnants and the Interstellar Medium*, ed. R. S. Roger & T. L. Landecker, *Proc. IAU Colloq.* No. 101 (Cambridge: Cambridge University Press), 331–334
- Reynolds, S. P. 1998, *ApJ*, 493, 375
- . 2004, *Advances in Space Research*, 33, 461
- . 2008, *ARA&A*, 46, 89
- . 2009, *ApJ*, 703, 662
- Reynolds, S. P., & Chevalier, R. A. 1981, *ApJ*, 245, 912
- Reynolds, S. P., & Gilmore, D. M. 1986, *AJ*, 92, 1138
- Reynolds, S. P., & Keohane, J. W. 1999, *ApJ*, 525, 368
- Reynoso, E. M., Moffett, D. A., Goss, W. M., et al. 1997, *ApJ*, 491, 816
- Ryu, D., Kang, H., Cho, J., & Das, S. 2008, *Science*, 320, 909
- Slane, P., Lee, S.-H., Ellison, D. C., et al. 2014, *ApJ*, 783, 33
- Sun, X. H., Reich, P., Reich, W., et al. 2011, *A&A*, 536, A83
- Uchiyama, Y., Aharonian, F. A., Tanaka, T., Takahashi, T., & Maeda, Y. 2007, *Nature*, 449, 576
- van Weeren, R. J., Röttgering, H. J. A., Brüggén, M., & Hoeft, M. 2010, *Science*, 330, 347
- Vink, J. 2012, *A&A Rev.*, 20, 49
- Vink, J., & Laming, J. M. 2003, *ApJ*, 584, 758
- Völk, H. J., Berezhko, E. G., & Ksenofontov, L. T. 2005, *A&A*, 433, 229
- Völk, H. J., Berezhko, E. G., Ksenofontov, L. T., & Rowell, G. P. 2002, *A&A*, 396, 649
- Warren, J. S., Hughes, J. P., Badenes, C., et al. 2005, *ApJ*, 634, 376
- Webb, G. M., Drury, L. O., & Biermann, P. 1984, *A&A*, 137, 185
- Williams, B. J., Borkowski, K. J., Ghavamian, P., et al. 2013, *ApJ*, 770, 129
- Zirakashvili, V. N., & Aharonian, F. 2007, *A&A*, 465, 695